Agenzia nazionale per le nuove tecnologie, l'energia
e lo sviluppo economico sostenibile

Ministero dello Sviluppo Economico

RICERCA DI SISTEMA ELETTRICO

Rapporto Tecnico sul comportamento di miscele bifase in generatori di vapore a tubi elicoidali con diverse geometrie ed in soluzioni alternative

M. Colombo, A. Cammi, J. De Amicis, M.E. Ricotti

Report RdS/2012/020

RAPPORTO TECNICO SUL COMPORTAMENTO DI MISCELE BIFASE IN GENERATORI DI VAPORE A TUBI ELICOIDALI CON DIVERSE GEOMETRIE ED IN SOLUZIONI ALTERNATIVE

M. Colombo, A. Cammi, J. De Amicis, M.E. Ricotti – CIRTEN, Politecnico di Milano

Settembre 2012

Report Ricerca di Sistema Elettrico
Accordo di Programma Ministero dello Sviluppo Economico - ENEA
Area: Governo, gestione e sviluppo del sistema elettrico nazionale
Progetto: Nuovo nucleare da fissione: collaborazioni internazionali e sviluppo competenze in materia nucleare
Responsabile del Progetto: Paride Meloni, ENEA

CIRTEN

Consorzio **I**nteruniversitario per la **R**icerca **TE**cnologica **N**ucleare

POLITECNICO DI MILANO

DIPARTIMENTO DI ENERGIA, Sezione INGEGNERIA NUCLEARE-CeSNEF

Rapporto Tecnico sul comportamento di miscele bifase in generatori di vapore a tubi elicoidali con diverse geometrie ed in soluzioni alternative

M. Colombo, A. Cammi, J. De Amicis, M.E. Ricotti

CERSE-POLIMI RL-1485/2012

Milano, Agosto 2012

Lavoro svolto in esecuzione della linea progettuale LP2– punto D.2b
AdP MSE-ENEA "Ricerca di Sistema Elettrico" - PAR2011
Progetto 1.3.1 – "Nuovo Nucleare da Fissione: collaborazioni internazionali e sviluppo competenze in materia nucleare".

INDEX

Executive Summary..... - 3 -

Part I

EXPERIMENTAL CHARACTERIZATION OF PRESSURE DROPS AND CHANNEL INSTABILITIES IN HELICAL COIL SG TUBES……

Part II

ASSESSMENT OF DIFFERENT TURBULENCE MODELS IN HELICALLY COILED PIPES THROUGH COMPARISON WITH EXPERIMENTAL DATA…….

Part III

SUPERPOSITION OF DWOs WITH LEDINEGG-TYPE INSTABILITIES……..……

APPENDIX – EXPERIMENTAL DATABASE……..

EXECUTIVE SUMMARY

This document presents the research activities carried out by Politecnico di Milano on the subject of single and two-phase flow behaviour in helical coil tubes for innovative steam generators. The R&D activities refer both to experimental campaigns, carried out at SIET labs, and modelling.

In Part I, single phase and two-phase flow are investigated, for pressure drops measurement and density waves and Ledinegg instabilities. The activity is a follow-up of the previous year investigation, where only few experimental points/operating conditions were analysed. The content of the research has been published as a scientific paper presented at ICAPP international conference.

In Part II, a CFD model is described, developed and validated versus experimental data obtained from the facility at SIET. The model will be used to simulate different geometries and boundary conditions for the helical coil tubes. Even in this case, the work has been published as a scientific paper presented at ICONE20 international conference.

Part III is specifically devoted to the description of the superposition of DWO type instability with Ledinegg type instability. This activity was required as a result of the experimental investigation at low pressure, where Ledinegg instability conditions occurred, thus a further investigation has been carried out.

In the Appendix, the main data of the experimental campaigns carried out during the year are reported.

1

PART I

Paper presented at:
ICAPP '12
Chicago, USA, June 24-28, 2012
Paper 12306

EXPERIMENTAL CHARACTERIZATION OF PRESSURE DROPS AND CHANNEL INSTABILITIES IN HELICAL COIL SG TUBES

Abstract - *Helical tube heat exchangers provide better heat transfer characteristics, an improved capability to accommodate stresses due to thermal expansions and a more compact design with respect to straight tube heat exchangers. For these advantages they are considered as an option for the Steam Generator (SG) of many new reactor projects of Generation III+ and Generation IV. In particular, their compactness fits well with the requirements of Small-medium Modular Reactors (SMRs) of integral design, where all the primary system components are located inside the reactor vessel.*

In this framework, thermal hydraulics of helical pipes has been studied in recent years by Politecnico di Milano in different experimental campaigns. Experiments have been carried out in a full-scale open loop test facility installed at SIET labs in Piacenza, Italy, to simulate the SG of a typical SMR. The facility includes two helical pipes (1 m coil diameter, 32 m length, 8 m height), connected via lower and upper headers. Following recently completed experimental campaigns dedicated to pressure drops and density wave instabilities, this paper deals with a new experimental campaign focused on both pressure drops (single-phase flow and two-phase flow, laminar and turbulent regimes) and flow instabilities. The availability of a large number of experimental data, in particular on two-phase flow, is of fundamental interest for correlation development, model validation and code assessment.

Two-phase pressure drops have been measured in adiabatic conditions, ranging from 200 to 600 kg/m^{2}s for the mass flux, from 30 to 60 bar for the pressure and from 0.1 to 1.0 for the flow quality. The channel characteristics mass flow rate - pressure drop has been determined experimentally in the range 10 - 40 bar, varying the mass flow rate at a fixed value of the thermal flux. In addition, single-phase pressure drops have been measured in both laminar and turbulent conditions. Density wave instabilities have been studied at mass flux from 100 to 400 kg/m^{2}s and pressure from 10 to 20 bar , to confirm the particular behavior of the stability boundary in helical geometry at low pressure and low mass flow rate. Finally, starting from the unstable regions identified from the experimental channel characteristics, Ledinegg

type instabilities have been investigated to drawn stability maps with complete stable and unstable regions in the dimensionless plane N_{sub}-N_{pch}.

I. INTRODUCTION

Helically coiled pipes are nowadays under study in the nuclear field as they are considered for the Steam Generators (SGs) of some new reactor projects of Generation III+ and Generation IV. If utilized for the SG, helical tubes provide better heat transfer characteristics, together with an improved capability to accommodate thermal expansions and the possibility of a more compact design. Compactness in particular fits well with new integral Small-medium Modular Reactors (SMRs) of Generation III+, in which SGs are located inside the reactor vessel[1]. The problem of the flow in a curved pipe was firstly addressed by Dean[2], who studied laminar flow in a toroidal pipe of small curvature with Navier-Stokes equations written in a cylindrical reference frame. In the following years the problem of single-phase flow has been deeply studied experimentally[3], analytically[4,5] and numerically[6,7], in both laminar and turbulent conditions. The various works available in literature on the subject have been comprehensively reviewed by Berger et al.[8], Shah and Joshi[9] and Naphon and Wongwises[10]. In an helical tube, curvature acts on the flow inducing a secondary motion on the channel cross section. Fluid particles flowing faster in the core region experience an higher centrifugal force and are pushed towards the outer wall. As a consequence, two counter-rotating vortices originate on the channel cross section and the fluid recirculation promotes higher heat transfer rates together with higher friction pressure losses.

With respect to single-phase flow, comparatively less papers have been published focused on two-phase flow, therefore the availability of experimental data becomes of utmost importance for advances on the study of the phenomena involved and for the development and validation of models and correlations. The Nuclear Engineering Division of the Politecnico di Milano has been involved for a long time in experiments focused on fluid flow in helically coiled pipes. Cioncolini and Santini[11,12] tested a large number of small helices of different curvature and small pitch, to study laminar to turbulent flow transition and single-phase[11] and two-phase pressure drops[12]. Two-phase diabatic pressure drops were also measured in a full scale open loop test facility, reproducing the SG tube of an integral SMR of Generation III+[13]. The same test section was also included in a closed loop circuit, to study a passive heat removal system operating in natural circulation[14]. The facility was recently renewed to test Density Wave Oscillations (DWOs) in parallel channels, by adding a second helical tube identical to the first one (same coil diameter, pitch and length). The two helices have been connected with common lower and upper headers, to provide the constant pressure drop boundary condition required for the instability inception[15].

This paper presents a new experimental campaign dedicated to both two-phase pressure drops and parallel channel instabilities. Aim of the experiments was to collect new experimental data to expand previous databases, enlarge the ranges of explored conditions and study in more detail some phenomena not adequately examined in the previous experiments. Firstly, single-phase pressure drops have been measured, adding data collected in an helical pipe of greater dimension and higher pitch to the database of Cioncolini and Santini[11]. Concerning two-phase pressure drops, experiments have been executed in adiabatic conditions, supplying to the preheater all the thermal power required to have two-phase mixture at the test section inlet. Only a small amount of thermal power was supplied to the test section, to balance the thermal losses. Data recorded cover the ranges 30 – 60 bar for the pressure, 200 – 600 kg/m^{2}s for the mass flux and 0.1 – 1.0 for the mixture quality.

As concerns two-phase flow parallel channel instabilities, DWOs are originated by enthalpy perturbations and respective delay propagations throughout the channel. The difference in density between the fluid entering the channel (subcooled liquid) and the fluid exiting (low density two-phase mixture) triggers delays in the transient distribution of pressure drops along the tube, which may lead to self-sustained oscillations[16,17]. DWOs show peculiar characteristics in helical geometry[15]. In particular, an increase in inlet subcooling does not preserve its destabilizing effect on the instability inception at low subcoolings, therefore the instability threshold does not exhibit the classical "L-shape" observable in straight pipes. On the contrary, inlet subcooling results strongly stabilizing at low subcoolings[15]. Deviations from the above described behavior were only observed at the lower values of system pressure and mass flux, at which the stability boundary seemed to agree better with the straight channel behavior described in literature[16]. For these reasons new experiments have been conducted, to study in more detail low system pressure and mass flux conditions, in particular at 10 and 20 bar for the pressure and from 100 to 400 kg/m^{2}s for the mass flux.

Finally, also Ledinegg type instability has been studied, in particular in the range from 10 to 40 bar for the system pressure. Only preliminary investigated in previous experiments, in this paper Ledinegg instability is characterized in details, in particular in regions where it partially superimposes on DWOs. Ledinegg type instability occurs when a channel is operated in the negative slope region of its pressure drop – mass flow rate characteristics. Flow excursion appears as the system is forced to reach a new operating point[16]. Regions potentially affected by Ledinegg instability were identified with channel characteristics, experimentally derived in the ranges 10 – 40 bar for the pressure, 50 – 1000 kg/h for the mass flow rate and 20 – 60 kW for the thermal power.

The experimental facility is described in Section II, Section III presents pressure drop results, divided in single-phase flow and two-phase flow, whereas instability experimental data and channel characteristics are presented in Section IV.

II. THE EXPERIMENTAL FACILITY

The experimental facility, built and operated at SIET labs, is provided with SG full elevation and is suited for the reproduction of prototypical thermal hydraulic conditions. Coil geometry is representative of the SG pipe dimensions of a typical SMRs of integral design, coil diameter is 1 m, while pipe inner diameter is 12.53 mm. Tube length is 32 m, whereas facility height is 8 m. Two identical helical pipes are included, connected with common lower and upper headers to provide the constant pressure drop boundary condition required for the study of parallel channel instabilities. The heated pipes, which implement the common simplification given by a constant heat flux boundary (via electrical power) instead of the real controlled temperature boundary, are thermally insulated by means of rock wool. Thermal losses were evaluated via runs with single-phase hot pressurized water flowing inside the SG and estimated as a function of the temperature difference between the external tube wall and the environment[13]. The conceptual sketch of the new facility is depicted in Fig. 1, whereas a global view is provided in Fig. 2. Geometrical data of the two helical pipes are listed in Table I.

The whole facility is made by a supply section and a test section. The supply section feeds demineralized water from a tank to the test section, by means of a centrifugal booster pump and a volumetric feed water pump. The flow rate is controlled by a throttling valve (V3) positioned downwards the feed water pump and after a bypass line. System pressure control is accomplished by acting on a throttling valve (V4) placed at the end of the test section. An electrically heated preheater is located before the test section, to reach the desired temperature at the inlet of the test

section. The test section is electrically heated via Joule effect by DC current, with the possibility to supply power separately to first 24 m and last 8 m.

TABLE I

Test section main data.

Tube material	SS AISI 316L
Tube inner diameter [mm]	12.53
Tube outer diameter [mm]	17.24
Coil diameter [mm]	1000
Coil pitch [mm]	800
Tube length [m]	32
Heated section length [m]	24
Riser length [m]	8
Steam generator height [m]	8

Each tube is provided at the inlet with a calibrated orifice (with a differential pressure transmitter) and a valve. The calibrated orifice is used to measure the flow rate in each channel and to visually detect the instability inception, while the valve is used to impose a concentrated pressure drop. V1 and V2 represent the total pressure drop (instrumented orifice + valve) introduced at the inlet of the two helical tubes, respectively.

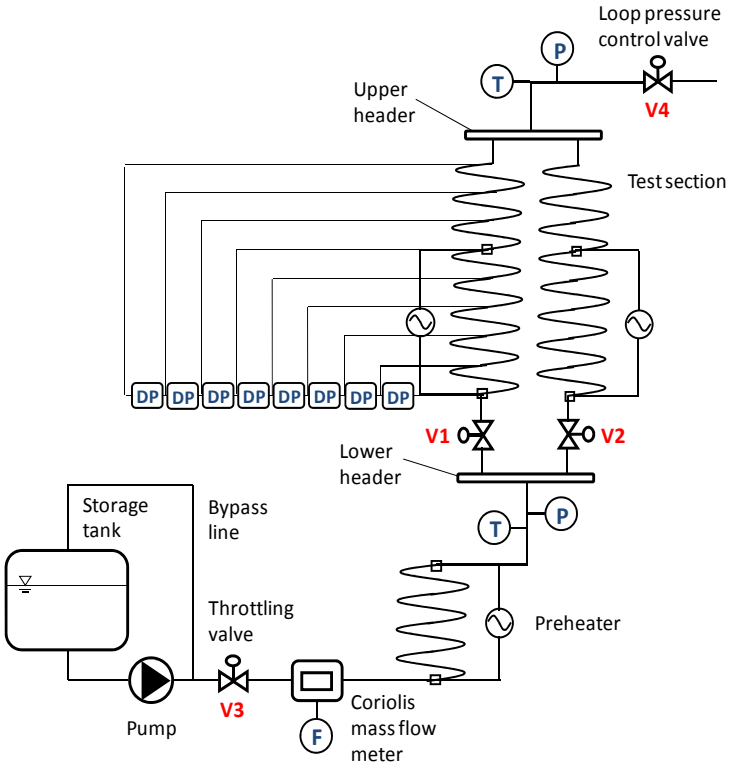

Fig. 1. Sketch of the experimental facility installed at SIET labs.

TABLE II

Pressure tap distribution along the test section (Channel A).

	Tap 1	Tap 2	Tap 3	Tap 4	Tap 5
Distance from tube inlet [m]	**0.20**	**5.17**	**9.19**	**13.15**	**17.14**
	Tap 6	**Tap 7**	**Tap 8**	**Tap 9**	
Distance from tube inlet [m]	**21.64**	**25.59**	**29.09**	**32.06**	

The pressure at inlet and outlet headers is measured by absolute pressure transducers; nine pressure taps are disposed nearly every 4 m along one tube and eight differential pressure transducers connect the pressure taps. Detailed distances between the taps are reported in Table II. An accurate measurement of the total flow rate is obtained by a Coriolis flow-meter, placed between the pump and the preheater. Bulk temperatures are measured with K-class thermocouples drowned in a small well at SG inlet and outlet headers. Wall thermocouples (K-class) are mounted throughout the two coils, with fining near the ends to identify the risk of dryout occurrence. Electrical power is obtained via separate measurement of current (by a shunt) and voltage drop along the test section (by a voltmeter). All the measurement

devices have been tested and calibrated at the certified SIET labs. A summary of the uncertainties is reported in Table III.

Pressure drops have been measured only in the pipe equipped with the pressure taps, while facility has been operated in the parallel channel configuration for instability experiments.

Fig. 2. Global view of the facility test section.

TABLE III

List of the uncertainties of physical quantities (referred to measurement values).

Water flow rate	± 1%
Fluid bulk and wall temperature	± 0.7 °C
Absolute pressure	± 0.1%
Differential pressure	± 0.4%
Supplied electrical power	± 2.5%
Evaluated thermal losses	± 15%

III. PRESSURE DROPS

III.A. Single-Phase Flow

Single-phase flow pressure drops have been tested in a wide range of Reynolds numbers to study the friction factor coefficient and the laminar to turbulent flow transition. Experiments have been conducted with water at ambient temperature and pressure, varying fluid inlet velocity to explore both laminar and turbulent regions (inlet velocity range: 0.1 – 2.25 m/s). Pressure drops due to friction have been calculated subtracting the gravitational term from total pressure loss experimental data. Darcy friction factor has been evaluated by:

$$f_D = 2 \cdot \frac{\Delta p_{\exp} \cdot d}{\rho \cdot w_{in}^2} \cdot \qquad (1)$$

Experimental friction factors have been compared to the work of Cioncolini and Santini[11], who tested a large number of helical pipes, characterized by different coil and pipe diameters and a small torsion. In particular, Fig. 3 compares the experimental data measured in the SIET facility with the data presented in [11] and relative to Coil8, which has the same coil diameter to pipe diameter ratio of our tube, i.e. almost the same coil curvature δ. As curvature plays the major role on friction pressure losses, data are almost overlapped, with friction coefficients from SIET facility slightly higher in the turbulent region. The last effect could be ascribed to torsion, which is significantly higher in our pipe. Accordingly to Yamamoto et al.[3], friction factor at a fixed curvature first increases with torsion (expressed with torsion parameter β_0) from that of a toroidal pipe, then it decreases toward that of a straight pipe as torsion further increases.

SIET facility, although it is characterized by an higher torsion with respect to the pipe tested by Cioncolini and Santini[11], has a torsion parameter $\beta_0 = 0.019$, which is not extremely high and belongs to the first region identified by Yamamoto et al.[3]

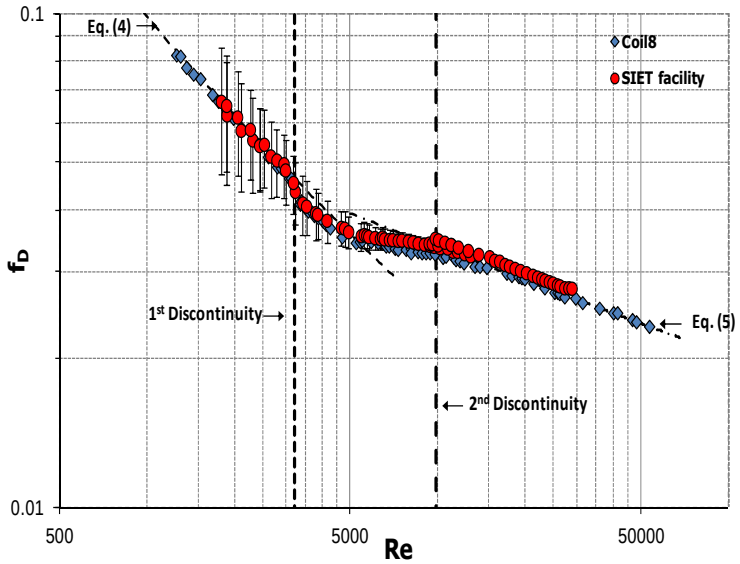

Fig. 3. Single-phase Darcy friction factors.

As observed by Cioncolini and Santini, the emergence of turbulence is a very smooth process in an helically coiled pipe and the Reynolds number necessary to have fully turbulent condition is higher with respect to a straight pipe. Two different discontinuities are encountered in the friction factor profile. A first discontinuity attests the emergence of turbulence, while a second discontinuity marks the end of the turbulence emergence process and the reaching of the fully turbulent flow condition. Between the two discontinuities, a slight depression in the friction factor profile is clearly observable. The two discontinuities are well predicted by the two following formulas[11]:

$$Re_1 = 12500 \cdot \left(\frac{D}{d}\right)^{-0.31}; \qquad (2)$$

$$Re_2 = 120000 \cdot \left(\frac{D}{d}\right)^{-0.57}. \qquad (3)$$

Friction factors are well predicted with the correlations proposed by Ito[18], for laminar and turbulent conditions respectively:

$$f_D = \frac{1376 \cdot \left(\frac{D}{d}\right)^{-0.5}}{\left[1.56 + \log_{10} \cdot \left(Re \cdot \left(\frac{D}{d}\right)^{-0.5}\right)\right]^{5.73}}; \qquad (4)$$

$$f_D = 0.304 \cdot Re^{-0.25} + 0.029 \cdot \left(\frac{D}{d}\right)^{-0.5}. \qquad (5)$$

III.B Two-Phase Flow

Two-phase friction pressure losses have been measured in the following operating conditions:

- pressure: 30, 40 and 60 bar;
- mass flux: 200, 400 and 600 kg/m^{2}s;
- flow quality: from 0.1 to 1.0.

Experiments have been made in adiabatic condition, therefore all the thermal power was supplied to the fluid in the preheater, to reach the desired inlet flow quality value. No thermal power was supplied to the test section, except for a small amount necessary to balance the thermal losses. Thermal losses were evaluated for preheater, connection pipes and test section as in the work of Santini et al.[13].
Two-phase pressure drops can be expressed with a steady-state momentum balance:

$$p_{in} - p_{out} = \Delta p_{fr} + \Delta p_{acc} + \Delta p_{grav}. \qquad (6)$$

Since experiments have been conducted in adiabatic conditions, therefore with an almost constant flow quality along the test section, the accelerative pressure term can be neglected and the balance equation reduces to friction and gravitational pressure losses, that is:

$$p_{in} - p_{out} = \frac{f_D}{2} \cdot \frac{G^2 \cdot L}{\rho_m \cdot d} + g \cdot \rho_m \cdot H \quad (7)$$

Adopting the homogeneous equilibrium model (adoption of a more complex two-phase flow model is foreseen in the near future) for the mixture, the homogeneous mixture density reads:

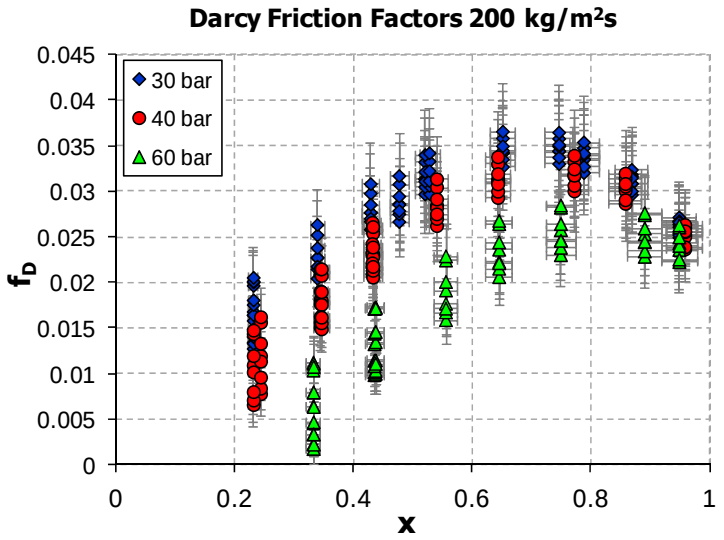

Fig. 4 Experimental friction coefficients at 200 kg/m^{2}s.

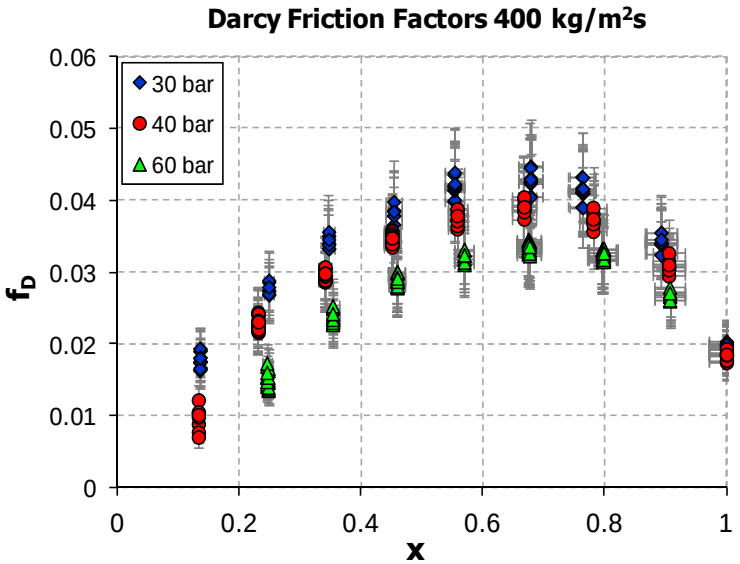

Fig. 5. Experimental friction coefficients at 400 kg/m^{2}s.

$$\rho_m = \left(\frac{1-x}{\rho_l} + \frac{x}{\rho_v} \right)^{-1}, \quad (8)$$

where x is the thermodynamic quality:

$$x = \frac{h - h_l}{h_v - h_l}. \quad (9)$$

Mixture enthalpy is calculated from an energy balance over the system preheater. The Darcy friction coefficient can be evaluated rearranging Eq. (7):

$$f_D = \frac{2 \cdot \rho_m \cdot d}{G^2 \cdot L} \cdot \left[(p_{in} - p_{out}) - g \cdot \rho_m \cdot H \right]. \quad (10)$$

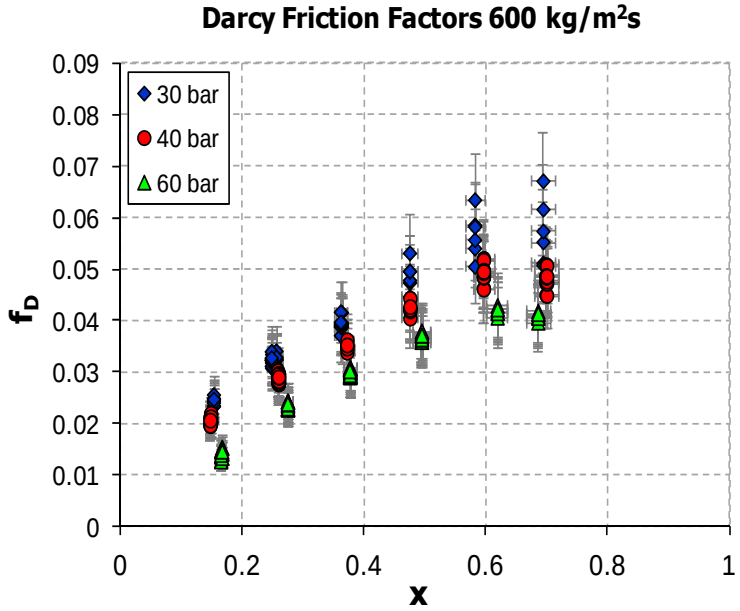

Fig. 6. Experimental friction coefficients at 600 kg/m^{2}s.

The friction coefficients (Fig. 4, Fig. 5 and Fig. 6) and consequently the pressure drops exhibit a parabolic shape, as they increase with flow quality up to an *x* value of about 0.7, to subsequently decrease if the flow quality is increased further. This behavior was previously observed also in the work of Santini et al.[13] and could be ascribed to an annular flow regime in which the liquid film becomes too thin to maintain the interface waves. Moreover, as expected, pressure drops decrease with pressure, keeping fixed system mass flow rate and flow quality.

IV. TWO-PHASE FLOW INSTABILITIES

IV.A Density Wave Oscillations

DWOs were tested in twin parallel channels to study low pressure and low mass flow rate conditions and verify the behavior of the stability boundary. Previous experiments[15] showed a stability boundary that deviates from the classical "L-shape" common to straight channels[16]. In particular, the effect of inlet subcooling was found to be stabilizing at low subcoolings, that is an increase of inlet subcooling through a decrease of water inlet temperature resulted in a more stable system. On the contrary, inlet subcooling is stabilizing at high subcoolings and destabilizing at low subcoolings

in straight channels. The "L-shape" behavior was partially recorded in helical pipes only at the lower values of pressure and mass flow rate tested, equal to 20 bar and 200 kg/m^{2}s. As a consequence, the new experiments have been performed at 10 and 20 bar and 100, 200 and 400 kg/m^{2}s, testing a wide range of inlet temperatures.

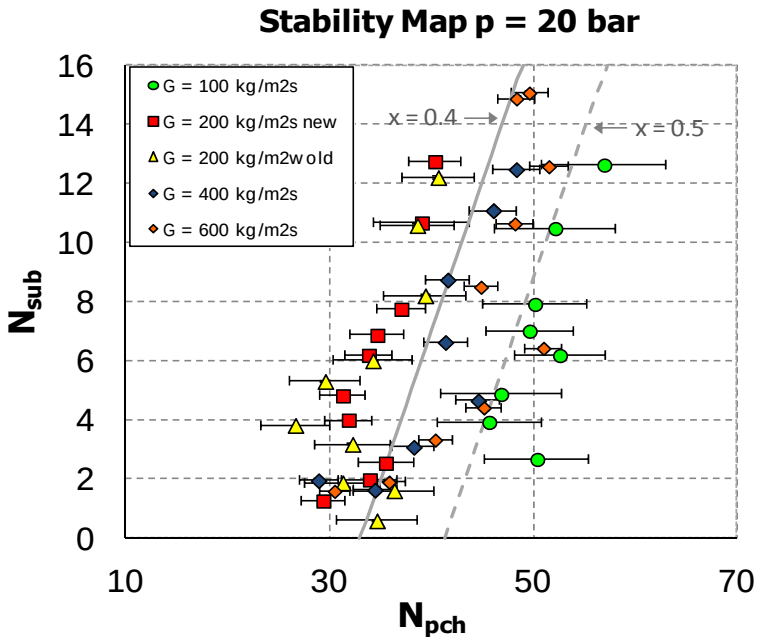

Fig. 7 Stability maps at 20 bar at different values of the mass flux (100, 200, 400, 600 kg/m^{2}s).

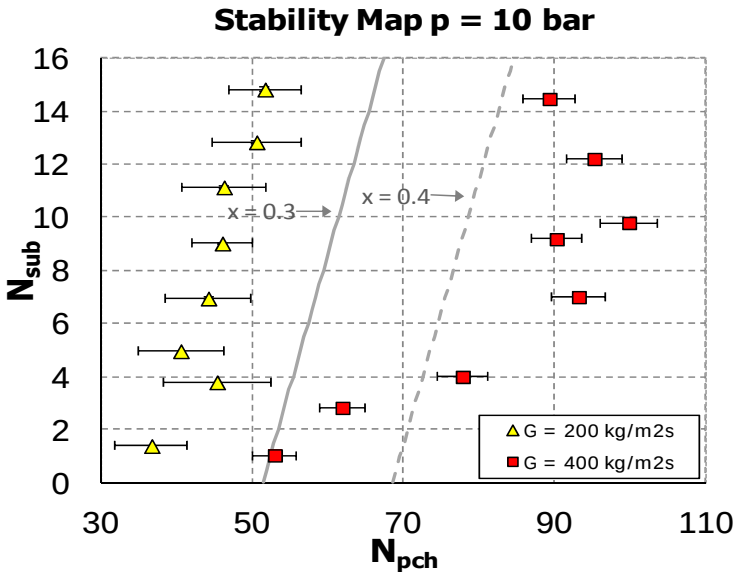

Fig. 8. Stability maps at 10 bar at different values of the mass flux (200 and 400 kg/m^{2}s).

Fig. 7 reports the stability maps at 20 bar in the dimensionless plane N_{sub}-N_{pch}[19]. New data at 100 and 200 kg/m^{2}s are reported together with previous data at 200, 400 and 600 kg/m^{2}s[15]. The subcooling stabilizing effect at low subcoolings is confirmed also at 20 bar and 200 kg/m^{2}s and 100 kg/m^{2}s, although the results are characterized by an higher uncertainty with respect to data at the higher mass flow rates. This is due to the lower thermal power required, which

causes an higher influence of the thermal loss uncertainties. In addition, an higher sensitivity characterizes the stability maps for low values of the system pressure. The same results are shown in Fig. 8, where stability maps at 10 bar and 200 and 400 kg/m^{2}s are depicted.

DWOs are characterized by waves of heavier and lighter fluid which travel alternatively along the boiling channel[16], therefore distinctive parameters are the period of oscillations and the period of oscillations over transit time ratio. Since two perturbations are required for each cycle, the period of oscillations is known from literature to be of the order of twice the mixture transit time. In particular, T is almost equal to twice the mixture transit time □ at high inlet subcoolings, and $T/$□ ratio is reduced by reducing the inlet subcooling[16]. In helical pipes instead, the period of oscillations over transit time ratio was found to be very low at high inlet subcoolings, moreover it increased reducing the subcooling number N_{sub}[15]. This characteristic behavior is confirmed also in the new experimental data, as it is shown in Fig. 9 and Fig. 10. Period of oscillations is found to be almost independent from inlet subcooling. Accordingly, $T/$□ ratio results considerably lower than one (~0.5) at high inlet subcoolings (when the fluid transit time in the heated channel is higher due to the long single-phase region), whereas it increases up to a value of nearly two as the inlet temperature approaches the saturation.

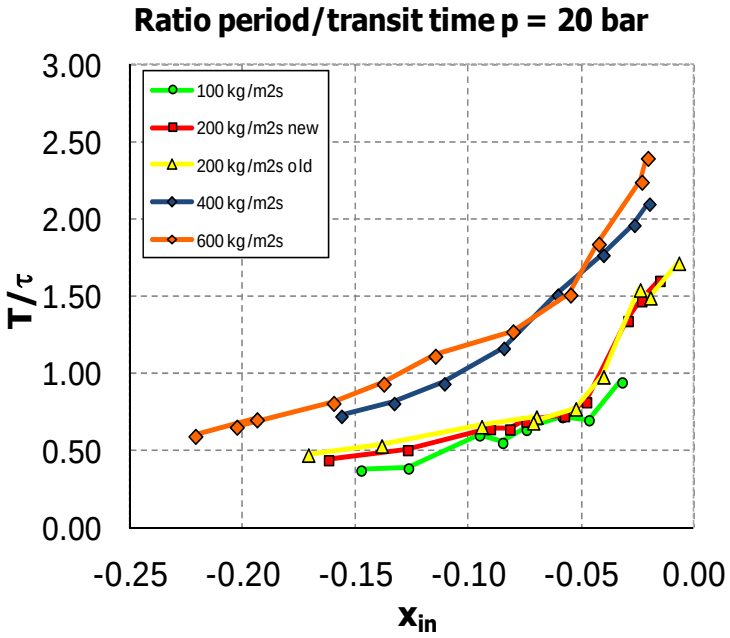

Fig. 9. Period of oscillation over transit time ratio at 20 bar as function of inlet subcooling and for different values of mass flux.

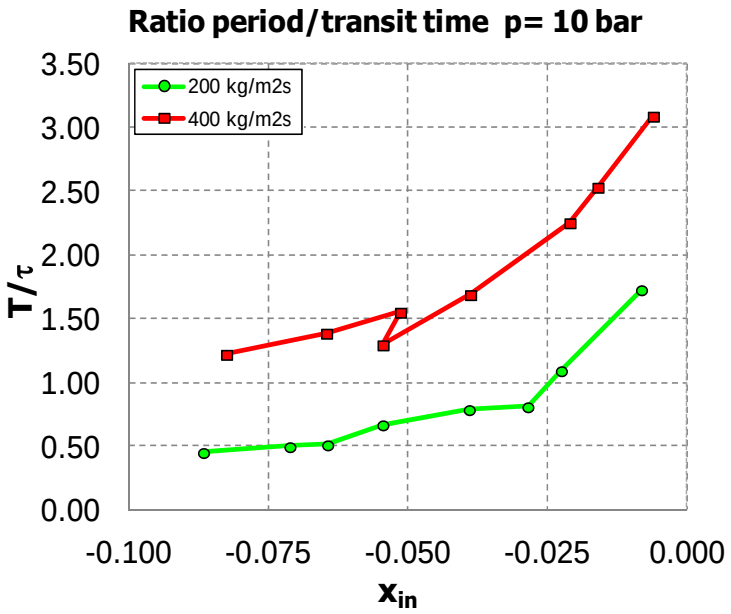

Fig. 10. Period of oscillation over transit time ratio at 10 bar as function of inlet subcooling and for different values of mass flux.

IV.B Ledinegg Instability

Ledinegg type instabilities were only partially studied in the past experiments, as flow excursions were observed during runs at the lowest pressure level (p = 20 bar), the highest mass flux (G = 600 kg/m^{2}s), and high inlet subcooling values (x_{in} < -15%). Ledinegg instability occurs when a heated channel operates in the negative slope region of the pressure drop versus flow rate curve (channel characteristics). In this respect, the boundary condition of constant pressure drop given by parallel channels acts as a flat pump external characteristics, forcing each channel into a wide flow excursion up to the reaching of new operating points on the internal characteristics.

Before the experiments on Ledinegg instabilities, channel characteristics has been determined experimentally in different system conditions to identify the negative slope regions necessary to trigger the flow excursion. In particular, pressure drops have been measured at 10, 20 and 40 bar, at inlet subcoolings -0.350 < x < -0.125 and thermal power between 20 kW and 60 kW, reducing the mass flow rate starting from a liquid outlet condition to reach high quality two-phase outlet condition. Fig. 11 shows channel characteristics in different system conditions. Negative slope regions have been successfully identified, moreover their amplitude increases reducing the inlet temperature (increasing the inlet subcooling) or increasing the thermal power. The most important effect is however due to the system pressure, which acts reducing negative slope region amplitude. From Fig. 11 it is possible to predict the appearance of Ledinegg instabilities at 10 and 20 bar, whereas a small number of unstable conditions could be expected at 40 bar, as a consequence of the smaller amplitude of the negative slope region.

Ledinegg instability occurs with marked flow excursions in the two parallel channels, as shown in Fig. 12. Flow excursion is evident, as Channel A flow rate increases. On the contrary, the flow rate in Channel B reduces proportionally to preserve the imposed total mass flow rate. The constant total pressure drop condition is respected

across the two tubes. Ledinegg instabilities are observed at a thermal power value much smaller with respect to DWOs and a further increase in thermal power allows to leave the unstable region.

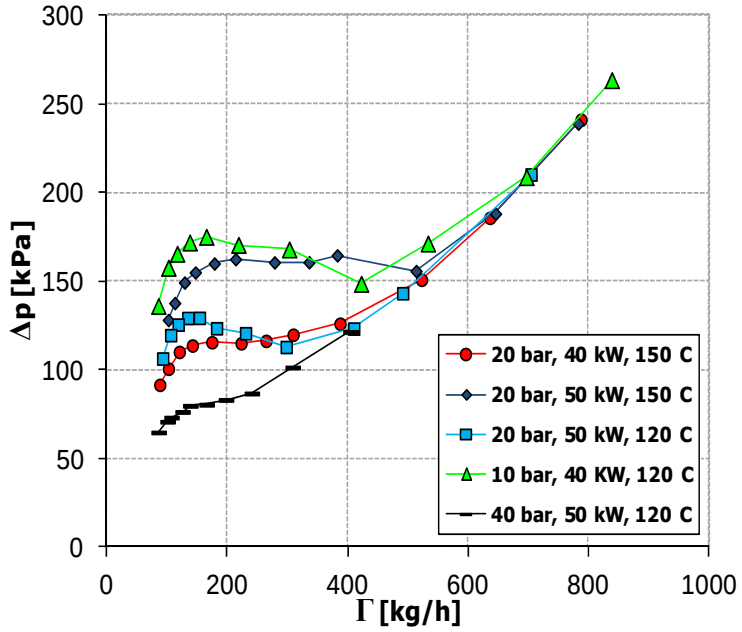

Fig. 11 Channel characteristics determined through experiments in different flow conditions.

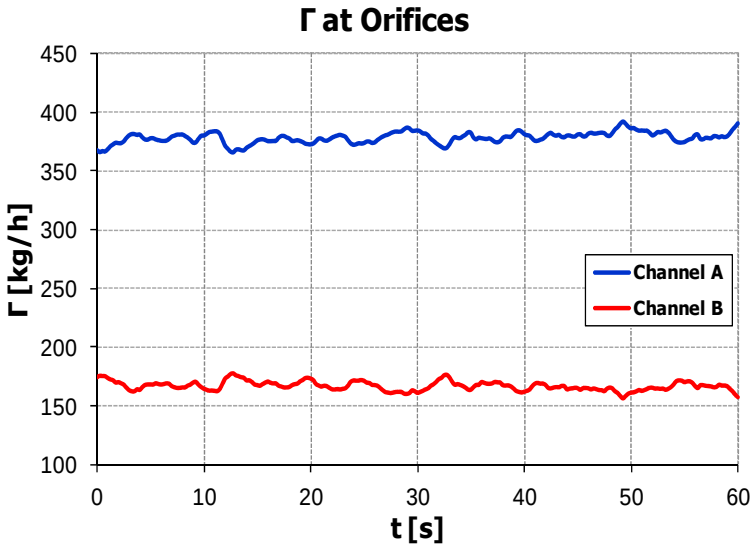

Fig. 12. Flow rate recorded in the two channels during a Ledinegg transient.
Data collected with: p = 20 bar; T_{in} = 135 °C; G = 600 kg/m^{2}s.
q = 67.5 kW (electrical power supplied per tube).

Fig. 13 reports a complete stability map in the N_{sub} – N_{pch} plane, including the DWO stability boundary and also the region affected by Ledinegg instability. Data were collected starting from a low thermal power condition with fixed system pressure, mass flow rate and inlet temperature. Power was gradually increased until the appearance of the flow excursion, then was further increased to leave Ledinegg region and reach the DWO stability boundary. For the same

value of system pressure and mass flow rate, the described procedure was repeated changing the inlet temperature to explore a wide range of inlet conditions. Data were collected at 20 bar and 400 and 600 kg/m^{2}s, 10 bar and 400 kg/m^{2}s (Fig. 14). Some experiments were also made at 40 bar and 400 and 600 kg/m^{2}s.

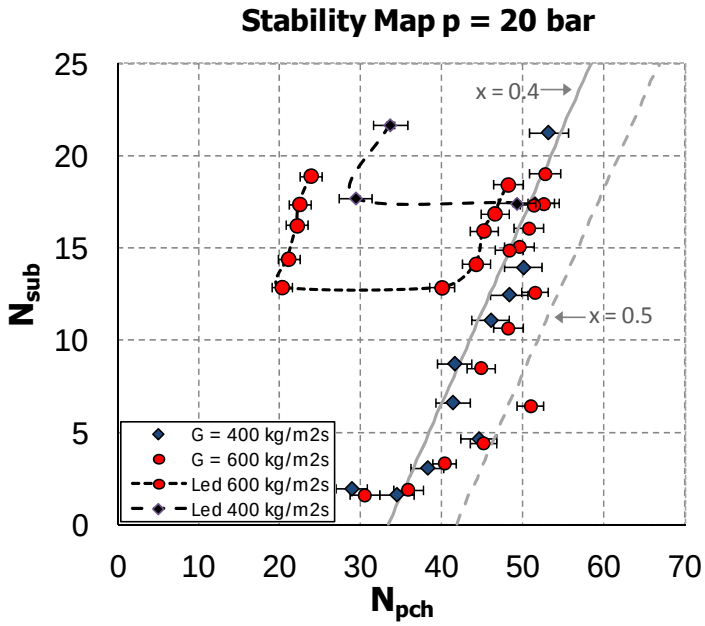

Fig. 13. Stability maps at 20 bar and 400 and 600 kg/m^{2}s with both DWO stability boundary and Ledinegg instability regions.

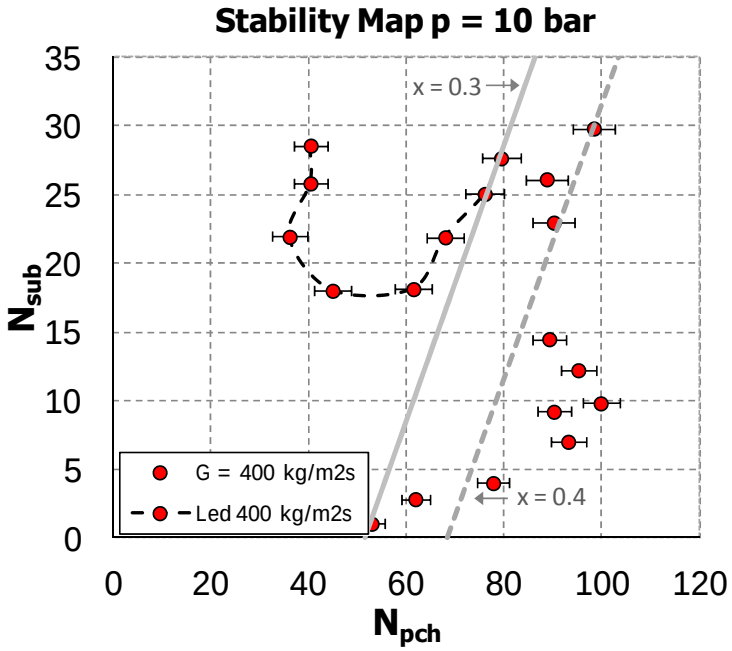

Fig. 14. Stability map at 10 bar and 400 kg/m^{2}s with both DWO stability boundary and Ledinegg instability region.

Ledinegg instabilities characterize regions of low thermal power and high inlet subcooling and they vanish increasing the thermal power before reaching the DWO stability boundary. Power difference between Ledinegg disappearance and DWOs is reduced increasing the inlet subcooling as the two instability modes tend to superimpose at very high inlet subcoolings. As a consequence, the complete stability boundary shows the typical "noose" shape reported in literature[16,20].

As anticipated observing channel characteristics, Ledinegg region widens increasing the inlet subcooling and also the mass flow rate, as it means an higher thermal power needed to reach the same flow quality condition. Also a decrease in system pressure promotes the instability, as it is possible to observe comparing unstable regions at 10 and 20 bar and 400 kg/m^{2}s. In agreement with the previous analysis, at 40 bar flow excursions were recorded only in a narrow range of system conditions.

V. CONCLUSIONS

Experimental data on single-phase pressure drops, two-phase pressure drops and two-phase flow parallel channel instabilities have been collected in a full-scale open loop test facility installed at SIET labs, in Piacenza. The experimental facility includes two helical pipes connected in parallel to reproduce the SG of a Generation III+ SMR of integral design. The availability of experimental data is of great importance for the development and validation of modeling tools to study the thermal hydraulics of helical pipes, in particular concerning two-phase flow.

Single-phase pressure drops have been measured in both laminar and turbulent flow conditions to enlarge a pre-existing database with data related to a pipe characterized by a significant pitch. Two-phase pressure drops have been measured in adiabatic conditions, giving all the thermal power to the preheater to have two-phase mixture already at the test section inlet. Only a small amount of power was provided to the test section to balance the thermal losses. Data have been collected in the ranges from 30 to 60 bar for the pressure, from 200 to 600 kg/m^{2}s for the mass flux and from 0.1 to 1.0 for the flow quality.

As concerns two-phase flow instabilities in parallel channels, DWOs are a dynamic type instability characterized by waves of "heavier" and "lighter" fluid propagating through the channel, triggered by delays in the transient distribution of the pressure drops along the pipe. New data allowed to confirm the particular behavior of the stability boundary in helical pipes also at low pressure and low mass flow rate, specifically at 10 and 20 bar and 100 and 200 kg/m^{2}s.

Also Ledinegg type instabilities have been characterized experimentally at 10, 20 and 40 bar and 400 and 600 kg/m^{2}s. Instability regions, located at low test section inlet temperatures, have been identified through experimental determination of negative slope regions in channel pressure drop-flow rate characteristics.

NOMENCLATURE

D	coil diameter [m]
d	pipe diameter [m]
f_D	Darcy friction factor coefficient
G	mass flux [kg/m^{2}s]
g	gravity acceleration [m/s^2]

H pipe height [m]
h entalphy [kJ/kg]
L pipe length [m]
N_{pch} phase change number
N_{sub} subcooling number
p pressure [Pa]
q thermal power [kW]
Re Reynolds number
T period of oscillations [s]
w velocity [m/s]
x thermodynamic quality
Γ mass flow rate [kg/s]
β_0 torsion parameter
δ dimensionless coil curvature
ρ density [kg/m^3]
τ transit time [s]

Subscripts

acc accelerative
exp experimental
fr friction
grav gravitational
in inlet
l liquid
m mixture
out outlet
v vapor

ACRONYMS

DWO Density Wave Oscillation
HEM Homogeneous Equilibrium Model
SG Steam Generator
SMR Small-medium Modular Reactor

REFERENCES

1. M. D. Carelli, L. E. Conway, L. Oriani, B. Petrovic, C. V. Lombardi, M. E. Ricotti, A. C. O. Barroso, J. M. Collado, L. Cinotti, N. E. Todreas, D. Grgic, M. M. Moraes, R.D. Boroughs, H. Ninokata, D. T. Ingersoll, F. Oriolo, "The Design and the Safety Features of the IRIS Reactor", *Nuclear Engineering and Design*, **230**, 151-167 (2004).
2. W. R. Dean, "Note on the Motion of Fluid in a Curved Pipe, *Philosopical Magazine*, **4**, 20, 208-223 (1927).

3. K. Yamamoto, T. Akita, H. Ikeuchi, Y. Kita, "Experimental Study of the Flow in a Helical Circular Tube", *Fluid Dynamics Research*, **16**, 237-249 (1995).

4. M. Germano, "On the Effect of Torsion on a Helical Pipe Flow", *Journal of Fluid Mechanics*, **125**, 1-8 (1982).

5. T. J. Huttl, R. Friedrich, R. Friedrich, "Influence of Curvature and Torsion on Turbulent Flow in Helically Coiled Pipes", *International Journal of Heat and Fluid FlowI,* **21**, 345-353 (2000).

6. G. Yang, M. A. Ebadian, "Turbulent Forced Convection in a Helicoidal Pipe with Substantial Pitch", *International Journal of Heat and Mass Transfer*, **39**, 10, 2015-2022 (1996).

7. J. S. Jayakumar, S. M. Mahajani, J. C. Mandal, K. N. Iyer, P. K. Vijayan, "CFD Analysis of Single-Phase Flows inside Helically Coiled Tubes", *Computers and Chemical Engineering*, **34**, 430-446 (2010).

8. S. A. Berger, L. Talbot, L. S. Yao, "Flow in Curved Pipes", *Annual Review of Fluid Mechanics*, **15**, 461-512 (1983).

9. R. K. Shah, S. D. Joshi, "Convective Heat Transfer in Curved Ducts. In: S. Kakac, R, K, Shah, W. Hung (Eds.), *Handbook of Single-Phase Convective Heat Transfer*, Chapter 3, Wiley Interscience, New York (1987).

10. P. Naphon, S. Wongwises, "A Review of Flow and Heat Transfer Characteristics in Curved Tubes", *Renewable and Sustainable Energy Reviews*, **10**, 463-490 (2006).

11. A. Cioncolini, L. Santini, "An Experimental Investigation Regarding the Laminar to Turbulent Flow Transition in Helically Coiled Pipes", *Experimental Thermal and Fluid Science*, **30**, 367-380 (2006).

12. A. Cioncolini, L. Santini, M. E. Ricotti "Subcooled and Saturated Water Flow Boiling Pressure Drop in Small Diameter Helical Coils at Low Pressure", *Experimental Thermal and Fluid Science*, **32**, 1301-1312 (2008).

13. L. Santini, A. Cioncolini, C. Lombardi, M. Ricotti, "Two-Phase Pressure Drops in a Helically Coiled Steam Generator", *International Journal of Heat and Mass Transfer*, **51**, 4926-4939 (2008).

14. L. Santini, D. Papini, M.E. Ricotti, "Experimental Characterization of a Passive Emergency Heat Removal System for a Gen III+ Reactor", *Science and Technology of Nuclear Installations*, **Vol. 2010**, doi: 10.1155/2010/864709, 12 pages (2010).

15. D. Papini, M. Colombo, A. Cammi, M. E. Ricotti, D. Colorado, M. Greco, G. Tortora, "Experimental Characterization of Two-Phase Flow Instability Thresholds in Helically Coiled Parallel Channels", *Proc. of the International Congress on Advances in Nuclear Power Plants*, Nice, France (2011).

16. G. Yadigaroglu, "Two-Phase Flow Instabilities and Propagation Phenomena", In: J.M. Delhaye, M. Giot, M.L. Riethmuller, *Thermohydraulics of two-phase systems for industrial design and nuclear engineering*, 353-396, Hemisphere Publishing Corporation, Washington (1981).

17. D. Papini, A. Cammi, M. Colombo, M. E. Ricotti, "On Density Wave Instability Phenomena: Modelling and Experimental Investigation", A. Ashan (Ed.), *Two-Phase Flow, Phase Change and Numerical Modeling,* InTech Publisher, Rijeka (2011).

18. H. Ito, "Friction Factors for Turbulent Flow in Curved Pipes", *Transaction of the American Society of Mechanical Engineering Journal of Basic Engineering*, **D81**, 123-124 (1959).

19. M. Ishii and N. Zuber, "Thermally Induced Flow Instabilities in Two-Phase Mixtures", *Proc. of the 4th International Heat Transfer Conference*, vol. 5, paper B5.11, Paris, France (1970).

20. W. Ambrosini, P. Di Marco, J.C. Ferreri, "Linear and Nonlinear Analysis of Density Wave Instability Phenomena", *International Journal of Heat and Technology*, **18**, *1*, 27-36 (2000).

Part II

Paper presented at:
20th International Conference on Nuclear Engineering
collocated with the
ASME 2012 Power Conference
ICONE20-POWER 2012
July 30 - August 3, 2012, Anaheim, California, USA

ASSESSMENT OF DIFFERENT TURBULENCE MODELS IN HELICALLY COILED PIPES THROUGH COMPARISON WITH EXPERIMENTAL DATA

Abstract

This paper deals with a comprehensive study of fully developed single-phase turbulent flow and pressure drops in helically coiled channels. To the aim, experimental pressure drops were measured in an experimental campaign conducted at SIET labs, in Piacenza, Italy, in a test facility simulating the Steam Generator (SG) of a Generation III+ integral reactor. Very good agreement is found between data and some of the most common correlations available in literature. Also more data available in literature are considered for comparison. Experimental results are used to assess the results of Computational Fluid Dynamics (CFD) simulations. By means of the commercial CFD package FLUENT, different turbulence models are tested, in particular the Standard, RNG and realizable k-ε models, Shear Stress Transport (SST) k-ω model and second order Reynolds Stress Model (RSM). Moreover, particular attention is placed on the different types of wall functions utilized through the simulations, since they seem to have a great influence on the calculated results. The results aim to be a contribution to the assessment of the capability of turbulence models to simulate fully developed turbulent flow and pressure drops in helical geometry.

INTRODUCTION

Helical pipes and helically coiled heat exchangers are widely used in different industrial applications such as power generation, nuclear industry, process plants, heat recovery systems, refrigeration, chemical and food industry. A renewed interest is nowadays characterizing the nuclear field, as helically coiled Steam Generators (SGs) are foreseen in different new reactor projects of Generation III+ and Generation IV. Better heat transfer characteristics, compactness and a greater capability to accommodate thermal expansions, held by helical pipes, could contribute to reach the goals fixed for next generation nuclear reactors, in particular with respect to performance improvement and cost reduction. Among others, compactness fits well with new Generation III+ Small-medium Modular Reactors (SMRs) of integral design [1], where the SGs and all the primary system components are located inside the reactor vessel. Growing interest has encouraged new studies focused on helical geometry, as further work is required to better understand some of the physical phenomena involved and apply to helical pipes some of the most advanced and complex simulation tools developed for straight pipes.

The paper is focused on the single-phase turbulent flow in helical pipes. Firstly, single-phase pressure drops were measured at SIET labs, in Piacenza, Italy, in a test facility which reproduces the SG of an integral SMR of Generation III+. Experimental data are firstly compared with the most common correlations available in literature. Then, different turbulence models extensively tested and calibrated in straight pipes are applied, to assess their predictions of pressure drops and friction factor coefficients.

The problem of the flow in curved pipes has been addressed by many researchers and the large amount of works available on the subject can be found in different literature reviews [2-4]. Dean first derived a solution for laminar flow in a toroidal pipe of small curvature with Navier-Stokes equations written in a cylindrical reference frame [5]. The flow exhibited a secondary flow pattern on pipe cross section, constituted by two symmetrical counter rotating vortices. Secondary motion is induced by curvature, as fluid particles flowing faster on core region experience an higher centrifugal force and are pushed towards the outer wall. The two vortices promote fluid recirculation and lead to higher heat transfer rates and higher friction pressure losses. Besides the Reynolds number, a new parameter was discovered to characterize magnitude and shape of the secondary motion, the Dean Number, defined as:

$$De = Re \cdot \sqrt{\frac{d}{D}} \tag{1}$$

In the following years different experimental studies were made [6-8] focused on both laminar and turbulent flow, leading to the development of numerous correlations able to predict the single-phase friction pressure drop [9-11]. The large number of correlations available has been reviewed in [12].

In the field of numerical study of turbulent flow, the standard k-ε turbulence model was firstly applied by Yang and Ebadian [13] to study fully developed turbulent flow and convective heat transfer in an helically coiled pipe of finite pitch. The same turbulence model was used in [14] to study turbulent developing heat transfer with FLUENT/UNS code as the numerical solver. Same authors addressed the effect of inlet turbulence on the development of flow and heat transfer [15]. Li et al. [16] simulated mixed convective heat transfer in the entrance region of helical pipes with the renormalization group (RNG) k-ε model. Kumar et al. [17] addressed the pressure drops and the heat transfer in a tube-in-tube helical coil heat exchanger with the standard k-ε turbulence model and the Computational Fluid Dynamics

(CFD) package FLUENT. Jayakumar et al. [18] evaluated the performance of an helically coiled heat exchanger with the realizable *k-ε* model implemented in the FLUENT code. More recently, the same turbulence model was used to study pressure drops and heat transfer in an helical pipe and the effect of different geometrical parameters on the results [19]. The authors developed a correlation to predict the local value of the Nusselt number.

In spite of the numerous works focused on CFD simulations of turbulent flow in helical geometry, many of which individually validated with experimental data or previous results, a comprehensive comparison between turbulence model results is lacking. In this paper different turbulence models are compared to evaluate their capability to predict the pressure drop and the friction factor coefficient. In particular, the standard, RNG and realizable *k-ε* models, the Shear Stress Transport (SST) *k-ω* model and the second order Reynolds Stress Model (RSM) were tested. Simulations were made through the CFD package FLUENT version 6.2 [20], after a grid sensitivity study. The assessment procedure is made through comparison with experimental data and some of the most common correlations available in literature. In addition to experimental data collected at SIET labs, also data presented by Cioncolini and Santini [21] and related to helical pipes of different curvature were used. Particular attention was given to the near wall treatment, which turns out to be a key parameter for the correct prediction of the friction pressure losses. Besides standard wall function and non-equilibrium wall function, also the enhanced wall treatment implemented in FLUENT, which solves the viscous sub-layer explicitly, was tested.

SINGLE-PHASE EXPERIMENTAL DATA

Experimental Facility

The experimental facility, built and operated at SIET labs, is provided with SG full elevation and is suited for prototypical thermal hydraulic condition reproduction. Coil geometry is representative of the SG pipe dimensions of a typical SMRs of integral design, coil diameter is 1 m while pipe inner diameter is 12.53 mm. Tube length is 32 m, whereas facility height is 8 m. Two identical helical pipes are included, connected with common lower and upper headers, as thermal hydraulic instabilities in parallel channels were tested recently [22]. The conceptual sketch of the facility is depicted in Fig. 1, whereas geometrical data of the two helical pipes are listed in Table 1.

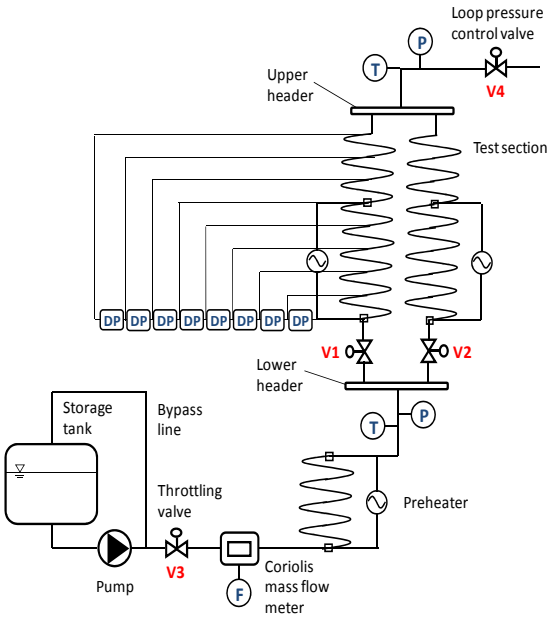

Figure 1 – Sketch of the experimental facility installed at SIET labs.

The whole facility is made by a supply section and a test section. The supply section feeds demineralized water from a tank to the test section, by means of a centrifugal booster pump and a volumetric feed water pump. The flow rate is controlled by a throttling valve (V3) positioned downwards the feed water pump and after a bypass line. System pressure control is accomplished by acting on a throttling valve (V4) placed at the end of the test section. An electrically heated preheater is located before the test section, and allows to create the desired temperature at the inlet of the test section. The test section is electrically heated via Joule effect by DC current, with the possibility to supply power separately to first 24 m and last 8 m.

Table 1 – Test section main data.

Tube material	SS AISI 316L
Tube inner diameter [mm]	12.53
Tube outer diameter [mm]	17.24
Coil diameter [mm]	1000
Coil pitch [mm]	800
Tube length [m]	32
Heated section length [m]	24
Riser length [m]	8
Steam generator height [m]	8

Table 2 – List of the uncertainties of the measured physical quantities.

Water flow rate	± 1%
Fluid bulk and wall temperature	± 0.7 °C
Absolute pressure	± 0.1%
Differential pressure	± 0.4%
Supplied electrical power	± 2.5%

Each tube is provided at the inlet with a calibrated orifice (with a differential pressure transmitter) used to measure the flow rate in each channel, and with a valve to impose a concentrated pressure drop. V1 and V2 represent the total pressure drop (instrumented orifice + valve) introduced at the inlet of the two helical tubes, respectively. The water pressures at lower and upper headers are measured by absolute pressure transducers; nine pressure taps are disposed nearly every 4 m along one tube and eight differential pressure transducers connect the pressure taps. An accurate measurement of the total flow rate is obtained by a Coriolis flow-meter, placed between the pump and the preheater. Bulk temperatures are measured with K-class thermocouples drowned in a small well at SG lower and upper headers. Wall thermocouples (K-class) are also mounted throughout the two coils. All the measurement devices have been tested and calibrated at the certified SIET labs. A summary of the uncertainties is reported in

Table **2**. Pressure drop measurements were made on the pipe equipped with the pressure taps.

Experimental Results

Single-phase pressure drops were tested in a wide range of Reynolds numbers to study the friction factor coefficient and the laminar to turbulent flow transition. Experiments were made with water at ambient temperature and pressure, varying fluid inlet velocity to explore both laminar and turbulent regions (inlet velocity range: 0.1 – 2.25 m/s). Pressure drops due to friction have been calculated subtracting the gravitational term from the total pressure loss. Darcy friction factor could then be evaluated by:

$$f_D = 2 \cdot \frac{\Delta p_{\exp} \cdot d}{\rho \cdot u_{in}^2} \tag{2}$$

Figure 2 shows experimental friction factors in both laminar and turbulent regions. Also data of Coil6 form the work of Cioncolini and Santini are reported [21], as they will be used in the comparison with CFD results. Coil6 has lower pipe and coil diameters and a slightly higher dimensionless coil curvature δ with respect to the SIET pipe. On the contrary, the SIET pipe presents higher dimensionless torsion τ and torsion parameter β_0. Geometrical data of the two pipes are compared in Table 3.

. Coil6 friction factors are slightly higher in the laminar region, in virtue of the higher coil curvature. Curvature effect is less important in the turbulent region, where Coil6 and SIET data are almost overlapped.

Table 3 – Geometrical parameters of the two pipes.

	SIET	**Coil6**
D [m]	1	0.3629
d [m]	0.01253	0.00681
δ	0.0116	0.0188
τ	0.002906	0.000329
β_0	0.0191	0.0017

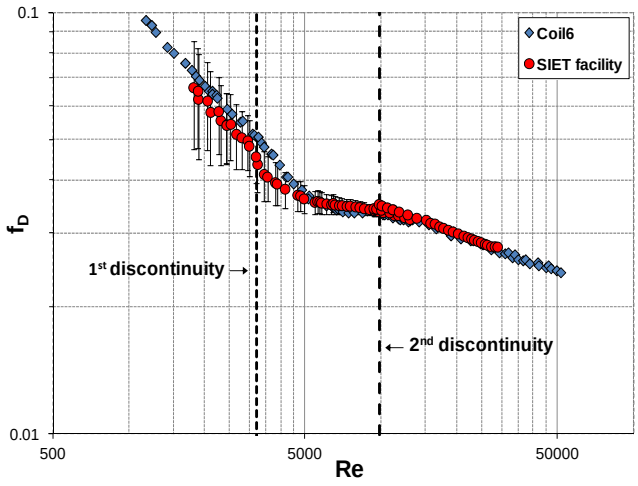

Figure 2 – Single-phase Darcy friction factors.

As observed in [21], the emergence of turbulence is a very smooth process in helically coiled pipes and the Reynolds number necessary to achieve fully turbulent condition is higher with respect to straight pipes. Two different discontinuities are observable in the friction factor profile. A first discontinuity attests the emergence of turbulence, while a second discontinuity marks the end of the turbulence emergence process and the reaching of fully turbulent flow condition. Between the two discontinuities, a slight depression in the friction factor profile is clearly observable. In the SIET pipe, the two discontinuities are well predicted by the two following formulas, proposed in [21]:

$$Re_1 = 12500 \cdot \left(\frac{D}{d}\right)^{-0.31} = 3216 \tag{3}$$

$$Re_2 = 120000 \cdot \left(\frac{D}{d}\right)^{-0.57} = 9886 \tag{4}$$

Many correlations are available in literature for the determination of the turbulent friction coefficient. In this work the correlations due to Ito [10], White [9] and Mishra and Gupta[11] are considered (Eq. (5), Eq. (6) and Eq. (7) respectively):

$$f_D = 0.304 \cdot Re^{-0.25} + 0.029 \cdot \left(\frac{d}{D}\right)^{0.5} \tag{5}$$

$$f_D = 0.32 \cdot Re^{-0.25} + 0.048 \cdot \left(\frac{d}{D}\right)^{0.5} \tag{6}$$

$$f_D = 0.3164 \cdot Re^{-0.25} + 0.03 \cdot \left(\frac{d}{D}\right)^{0.5} \tag{7}$$

Comparison between correlations and experimental data is provided in Fig. 3. For simplicity, correlations are only related to SIET pipe. Results for the two pipes are resumed in Table 4.

Table 4 – Errors between the correlations and the experimental data.

	Siet [%]			**Coil6 [%]**		
	Ito	White	M.&G.	Ito	White	M.&G.
Avg. Turb.	3.75	7.50	1.12	0.69	14.05	4.14
Max. Turb.	5.15	9.91	3.01	2.18	15.94	6.27
Avg. Trans.	3.77	13.45	7.13	6.09	17.28	9.60

Max. Trans.	8.99	17.85	11.12	10.75	23.62	15.19

Ito and Mishra and Gupta correlations agree very well with the experimental data, with average errors always lower than 5% and maximum errors that do not exceed the 7%. Results are satisfactory also in the transition region, where the average error is always lower than 10%. On the other hand, White correlation overestimates the friction factor coefficient. Due to its large application in literature, the Ito correlation will be considered in the following for the comparison with CFD results.

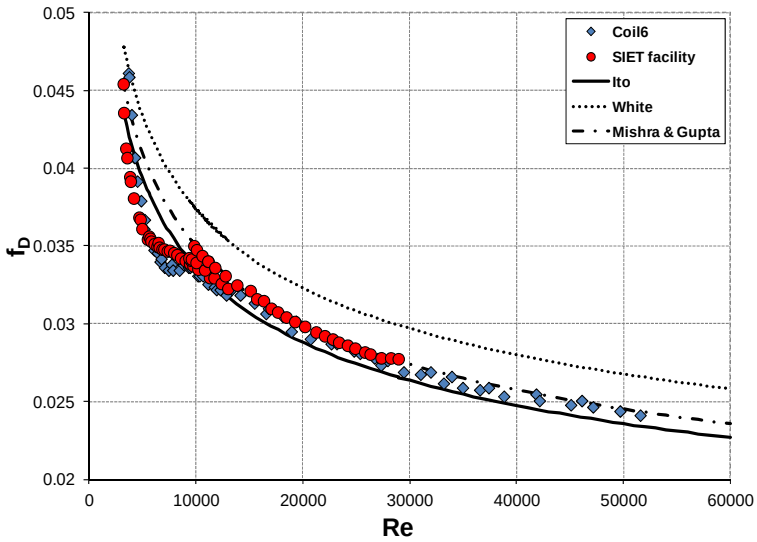

Figure 3 – Comparison between the experimental friction factors and the literature correlations.

CFD MODELING

5 different turbulence models were tested. The standard *k-ε* model proposed by Jones and Launder [23], with the same constant values recommended by the authors. The RNG *k-ε* model proposed by Yakhot and Orszag [24], derived using the mathematical technique called Renormalization Group method [25]. The model provides an analytical formula for the turbulent Prandtl number, includes the effect of swirl on turbulence and an analytically derived differential formula for effective viscosity, making it more accurate and reliable for rapidly strained flows, swirling flows and low Reynolds number flows. The realizable *k-ε* model [26] includes a new formulation for the turbulent viscosity and a new transport equation for the dissipation rate *ε*, derived from an exact equation for the transport of the mean-square vorticity fluctuations. The model is known to provide better performances for flows involving rotation, boundary layer under strong adverse pressure gradients, separation, recirculation and complex secondary flow features.

The SST *k-ω* model, proposed by Menter [27], applies the *k-ω* formulation in the inner part of the boundary layer to make the model directly usable all the way down to the wall through the viscous sub-layer. In addition the SST formulation switches to a *k-ε* behavior in the free stream.

The second order RSM involves calculation of the individual Reynolds stresses, using differential transport equations. The individual Reynolds stresses are then used to obtain closure of the Reynolds averaged momentum equation. More details on the model formulation can be found in [28,29].

The FLUENT code allow to choose between two modeling approaches to solve the near wall region of a turbulent flow, the wall function approach and a near wall model in which the near wall region is completely resolved all the way to the viscous sub-layer. Both approaches were tested to compare their results.

With the wall function method, the viscosity affected region and the fully turbulent region are bridged with semi-empirical formulas and the viscosity affected inner region is not resolved. Two types of wall function were tested, the standard two-layer based wall function [23] and the non-equilibrium wall function [30]. In both cases, the expression for velocity in the region between the wall and the first mesh node reads:

$$u / u^* = y^+ \qquad y^+ < 11.225 \qquad (8)$$

$$u / u^* = \frac{1}{K} \cdot ln\left(E \cdot y^+\right) \qquad y^+ \geq 11.225 \qquad (9)$$

The non-equilibrium wall function adds to the standard treatment a sensitivity of the mean velocity log-law to pressure gradient effects.

On the other hand, the FLUENT enhanced wall treatment considers a two layer model in which the viscosity affected near wall region is resolved all the way to the viscous sub-layer, provided that the mesh is sufficiently fine.

Grid and numerical settings

The commercial CFD package FLUENT was used for the simulations. Momentum and turbulence model equations were discretized using the second order upwind scheme and the SIMPLEC algorithm was used to resolve the coupling between velocity and pressure. Convergence criterion used was 10^{-5} for velocities and 10^{-4} for k, ε, ω and Reynolds stresses.

An helical pipe section geometrically identical to the one installed at SIET labs was simulated. Length of the pipe (about 3/4 of a turn) guarantees fully developed turbulent conditions, together with the correct evaluation of the pressure drop and the friction factor coefficient in the fully developed region. It must be noticed that fully developed conditions are reached within a shorter tube length with respect to straight pipes and the flow could be considered fully developed in about a quarter of a turn. At the inlet, uniform profiles for all the dependent variables were employed:

$$u = u_0, \quad k = k_0, \quad \varepsilon = \varepsilon_0 \qquad (10)$$

Pressure is fixed in the outlet section, no-slip boundary conditions are imposed at the wall and turbulence intensity I and the turbulence characteristic length scale L are imposed in the inlet section. In particular, I is defined as $u'/u \cdot 100\%$ and L is set to be $0.07 \cdot (d/2)$. A structured (block structured) grid was implemented to discretize the governing equations, with five blocks applied to form the helically coiled pipe as shown in Fig.4. The same geometry and grid were developed to reproduce the Coil6 of the work of Cioncolini and Santini [21], scaling dimensions with the correct geometrical parameters.

Two different grid independence study were carried out to define the correct grid to be used with the wall function approach and with the enhanced wall treatment. In fact, it is well known that although FLUENT uses the linear

(laminar) law when y^+<11.225, the first grid point should be located far enough to avoid a fine mesh in the near wall region, as the wall function cease to be valid in the viscous sub-layer.

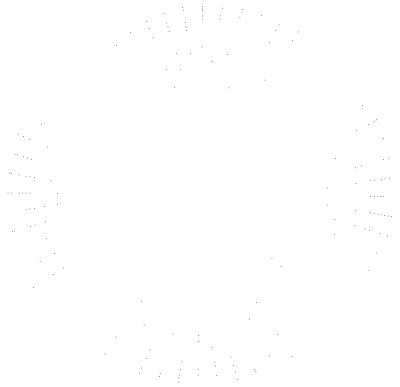

Figure 4 – Grid used for the SIET pipe with the wall function approach.

On the contrary, the enhanced wall treatment needs a first grid point y^+ value well inside the viscous sub-layer (y^+< 4 - 5) at least, with a most ideally value of the order of y^+=1. In the following, grid related to the wall function approach will be referred as mesh 1, while grid related to the enhanced wall treatment as mesh 2.

For mesh 1, 6 different grids were considered respectively for SIET pipe and Coil6. The results, obtained with the *k-ε* model with standard wall function, are resumed in Table 5. In both coils, at the beginning the grid refinement seems to have no effect, as the friction factor coefficient remains almost constant, then it starts to increase when the number of grid nodes is increased further. The latter effect clearly indicates how an excessively fine mesh in the near wall region is unsuited for the wall function approach. Grid selected were 1125 x 240 and 605 x 280 for the two cases respectively, as they allow to obtain more detailed definition of all the other physical quantities of interest in addition to the friction factor coefficient.

Table 5 – Grid independence study for mesh 1.

SIET pipe		**Coil6**	
Grid	f_D	Grid	f_D
405 x 240	0.0266	245 x 224	0.0268
720 x 240	0.0270	405 x 224	0.0265
1125 x 240	0.0275	605 x 280	0.0265
2000 x 240	0.0323	605 x 320	0.0266
2420 x 240	0.0339	1125 x 280	0.0273
4500 x 240	0.0380	2000 x 280	0.0306

Mesh 2 was determined for both SIET pipe and Coil6 with the realizable *k-ε* model and the results are resumed in Table 6. Refining the grid, friction factor coefficient lowers until the difference with the values calculated with the next finer

grid becomes negligible. Grid selected to be used with the enhanced wall treatment are 4500 x 240 and 3125 x 280 respectively.

Table 6 – Grid independence study for mesh 2.

SIET pipe		**Coil6**	
Grid	f_D	Grid	f_D
1125 x 240	0.0372	605 x 280	0.0288
2420 x 240	0.0367	1125 x 280	0.0291
3125 x 240	0.0358	2000 x 280	0.0297
4500 x 240	0.0341	3125 x 280	0.0300
5120 x 240	0.0340	4500 x 280	0.0300

RESULTS AND DISCUSSION

Figure 5 and Figure 6 compare the friction factor experimental data with the simulations from the three *k-ε* models with the standard wall function. The results are satisfactory for medium-high Reynolds numbers, where results of all the three models are almost overlapped and deviations from the experimental values and the Ito correlation are under 10% on average (Figure 5).

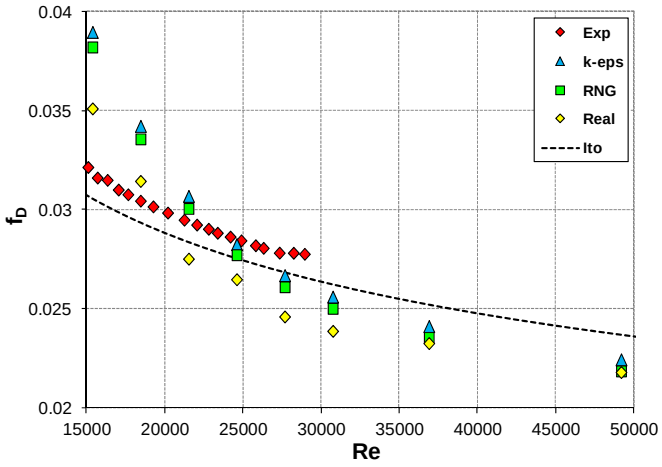

Figure 5 - Comparison between experimental data, Ito correlation and *k-ε* models with standard wall function for the SIET pipe in the medium-high Reynolds number region.

For medium-low Reynolds numbers, on the contrary, the *k-ε* models highly overestimate the friction factor coefficient, not only in the transition region, where the CFD friction coefficients have values approximately double with respect to experimental measurements, but also in the first section of the fully turbulent region. The results of the standard *k-ε* model could be considered satisfactory starting from Reynolds numbers up to 20000, as both the model and the standard wall function are known to provide better predictions at high Reynolds numbers. The results of the RNG *k-ε* model do not differ remarkably from the standard *k-ε*, so the comments previously made could be extended to the RNG model, which also becomes reliable starting from a Reynolds number of about 20000.

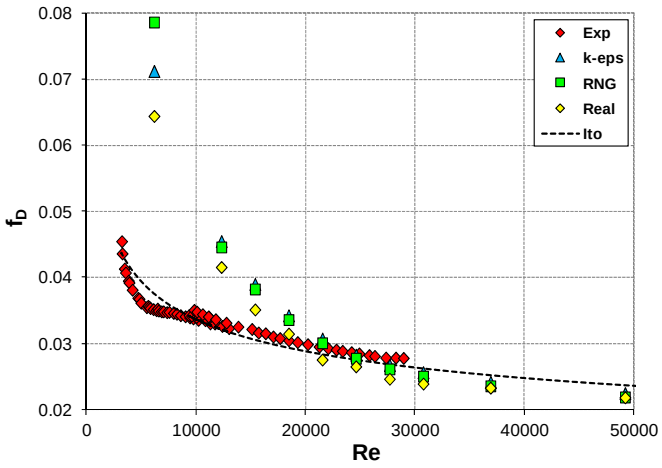

Figure 6 – Comparison between experimental data, Ito correlation and *k-ε* models with standard wall function for the SIET pipe.

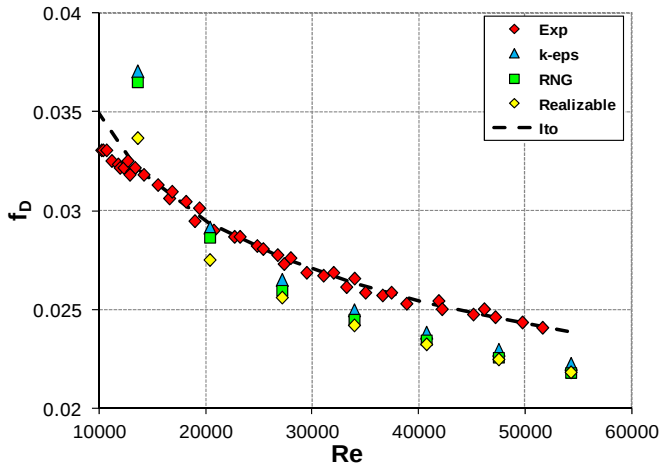

Figure 7 - Comparison between experimental data, Ito correlation and *k-ε* models with standard wall function for Coil6.

Slightly better results are given by the realizable *k-ε* model, which predicts a lower friction factor coefficient at low Reynolds numbers and shows satisfactory results also in the region $15000 < Re < 20000$. The overestimation of f_D in the low Reynolds number region seems strictly related to the wall function approach, as the dimensionless distance between the first grid point and the wall reduces with the Reynolds number down to values belonging to the viscous sub-layer. Similar results are found for Coil6 (Figure 7), with friction pressure losses overestimated up to Reynolds values of 15000 for the realizable model and about 20000 for the standard *k-ε* and the RNG models. Deviations from experimental data in the medium-high Reynolds number region remains under 10%.

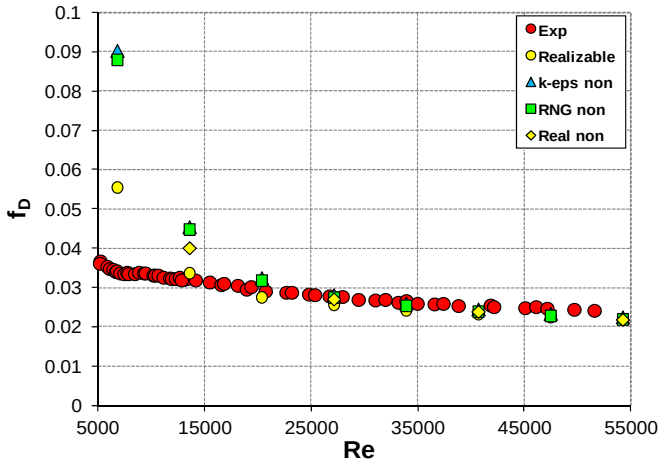

Figure 8 - Comparison between experimental data, realizable *k-ε* model with standard wall function and *k-ε* models with non-equilibrium wall function for Coil6.

Worse results are obtained with the non-equilibrium wall function. As a matter of fact friction factors do not differ with respect to the standard wall function for medium-high Reynolds, whereas deviations from experimental data become higher in the low Reynolds number region. Figure 8 shows results for the three *k-ε* models.

RSM introduces an higher degree of detail and complexity with respect to the *k-ε* model. Results obtained with the RSM and standard and non-equilibrium wall functions are resumed in Figure 9. No significant differences are found with respect to the realizable *k-ε* model, in both low and high Reynolds number regions. Also in this case, the non-equilibrium wall function worsens the model behavior at low Reynolds numbers. It seems that the higher complexity and computational expense introduced with the RSM are not justified, at least as long as the wall function approach is adopted in the near wall region.

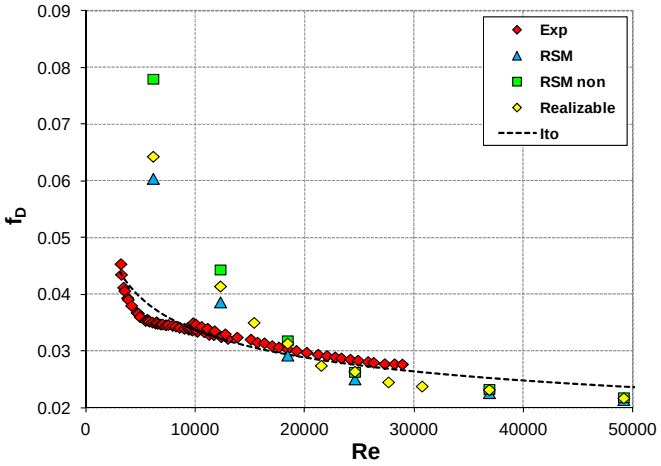

Figure 9 - Comparison between experimental data, realizable *k-ε*, RSM with standard wall function and RSM with non-equilibrium wall function for the SIET pipe.

To sum up, the realizable *k-ε* model with the standard wall function provides the best results, although the wall function approach seems to be unable to correctly predict the friction factor coefficient for low-medium Reynolds numbers. In

addition, also at high Reynolds the friction losses result slightly underestimated and the errors, even though satisfactory, are a little higher with respect to the Ito correlation. In virtue of the previous results, realizable *k-ε* model was chosen to perform the grid independency study for mesh 2, as pointed out previously.

Figure 10 shows CFD friction factors related to the 3 *k-ε* models when the near wall region is solved with the enhanced wall treatment. The agreement with experimental data is very good also at low Reynolds numbers, only in the first section of the transition region the friction factor is slightly overestimated. In the fully turbulent region the simulation results are improved with respect to the wall function approach, and deviations from the experimental data are negligible and comparable or slightly better with respect to the Ito correlation.

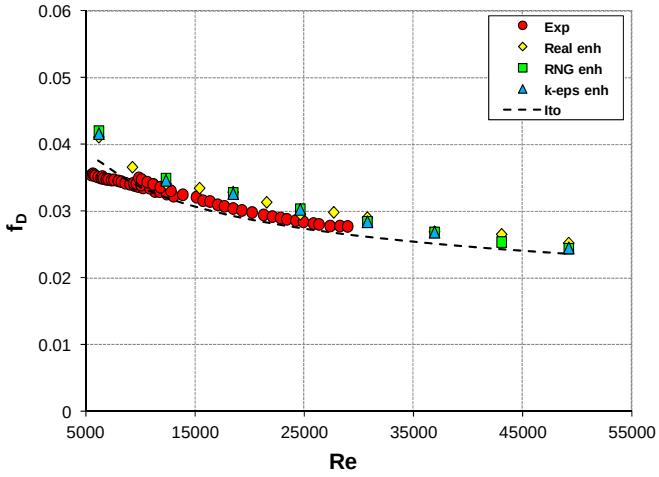

Figure 10 - Comparison between experimental data, Ito correlation and *k-ε* models with enhanced wall treatment for the SIET pipe.

Similar behavior is shown for Coil6 (Figure 11), although higher differences between the simulation results and the experimental data appear. Higher errors, although decreasing with the Reynolds number, seems to indicate an effect on error of the pipe curvature. Between the different models, the realizable *k-*ε provides slightly better results also with the enhanced wall treatment.

Also the SST *k-ω* model solves the near wall region all way down to the wall, so it is compared with the realizable *k-ε* model in Figure 12 for the SIET pipe and in Figure 13 for Coil6. At low Reynolds numbers, *k-ω* friction factors agree better with the experimental data, whereas at medium-high Reynolds the model overestimates the pressure losses.

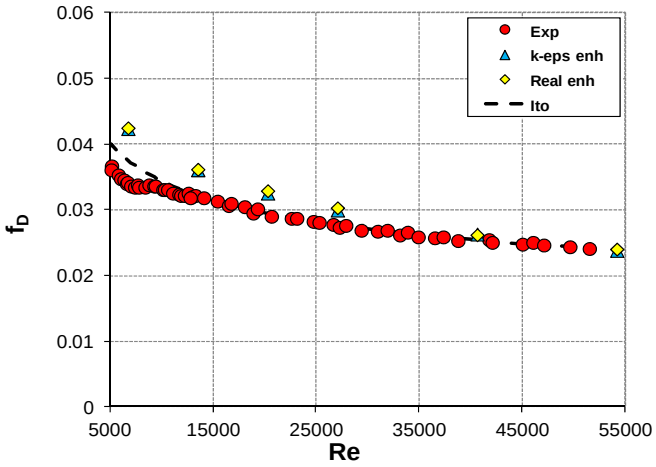

Figure 11 - Comparison between experimental data, Ito correlation, standard *k-ε* model and realizable *k-ε* model with enhanced wall treatment for Coil6.

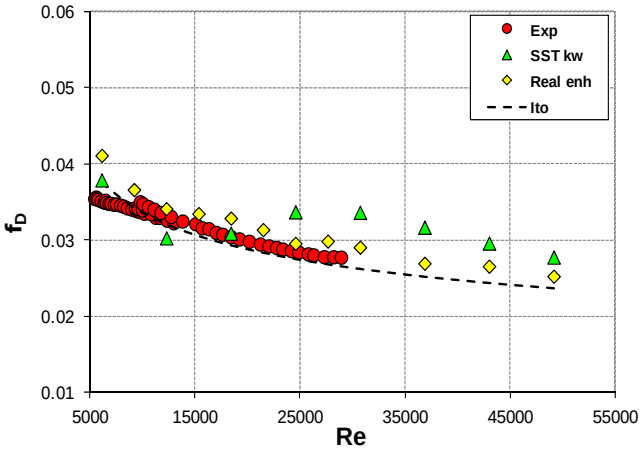

Figure 12 - Comparison between experimental data, Ito correlation, realizable *k-ε* model with enhanced wall treatment and SST *k-ω* model for the SIET pipe.

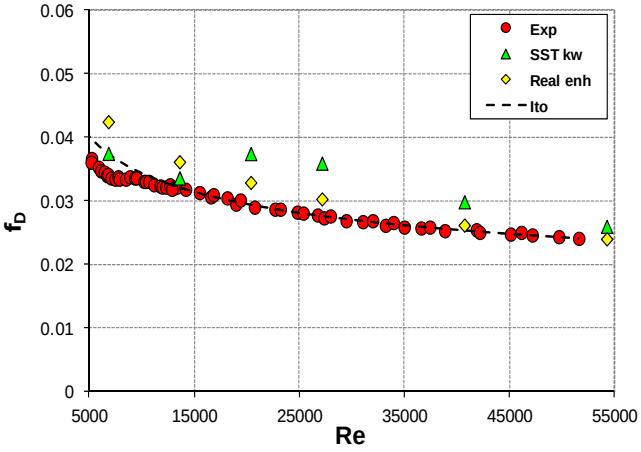

Figure 13 - Comparison between experimental data, Ito correlation, realizable *k-ε* model with enhanced wall treatment and SST *k-ω* model for Coil6.

To sum up, better results are still provided by the realizable *k-ε* model. In addition, the enhanced wall treatment seems to be able to describe in more details the little asymmetry of the two vortices due to the torsion effect in the SIET pipe (**Figure 14**).

As expected, the wall shear stress behavior is different with respect to straight pipes for the effect of the coil geometry and the secondary motion, shown in Figure 15. It is interesting to compare shear stress profiles obtained with the wall function and with the enhanced wall treatment. The analysis is focused on the realizable *k-ε* model, but it could be applied to all other turbulence models involving the use of the wall functions. Wall shear stress, as expected, is higher in the outer region of the pipe, where the velocity is higher for the centrifugal force effect induced by the tube geometry. A lower shear stress peak corresponds to the inner region of the pipe, where the velocity is lower.

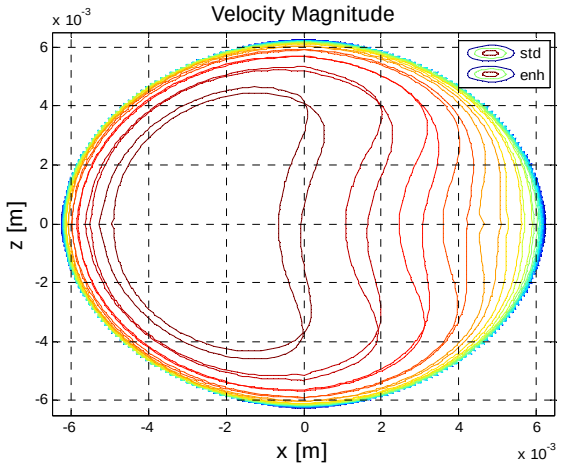

Figure 14 - Velocity magnitude profiles calculated with the realizable *k-ε* model with enhanced wall treatment and standard wall function.

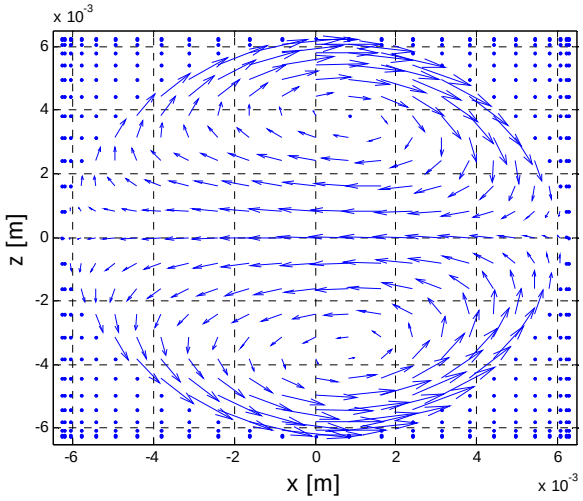

Figure 15 – Secondary flow in the pipe cross section obtained with CFD simulations.

Wall shear stress profile predicted with the enhanced wall treatment appears very smooth, with two discontinuities corresponding to higher and lower pipe regions, more evident at higher Reynolds. In the high Reynolds number region

(Figure 16), wall shear stress profiles are qualitatively similar, with higher values corresponding to the enhanced wall treatment.

Starting from medium Reynolds numbers, wall shear stress related to the standard wall function increases to exceeds the enhanced wall treatment values in the low Reynolds number region (Figure 17). Moreover, standard wall function profiles show different peaks in correspondence of outer, inner, higher and lower regions of the pipe. This effect is directly related to the use of wall functions, as the dimensionless distance from the wall y^+ is no more constant along the pipe circumference as in straight pipes, but it varies as a consequence of the secondary flow (Figure 18).

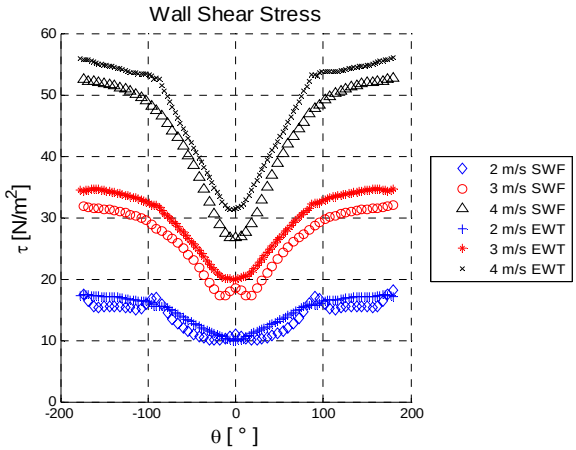

Figure 16 – Wall shear stress in the medium-high Reynolds number region (SWF=Standard Wall Function, EWT=Enhanced Wall Treatment).

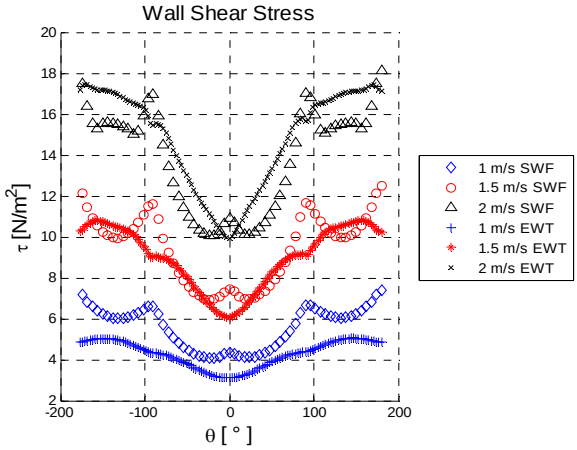

Figure 17 - Wall shear stress in the medium-low Reynolds number region (SWF=Standard Wall Function, EWT=Enhanced Wall Treatment).

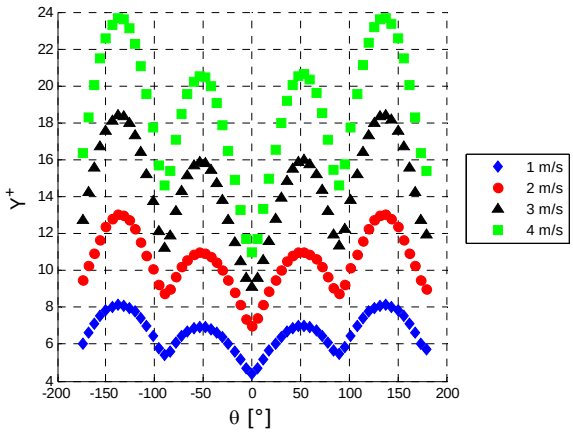

Figure 18 – Circumferential y^+ profile for the realizable *k-ε* model with standard wall function.

As a consequence, y^+ shows lower peaks ending in the viscous sub-layer also when its average value is sufficiently higher. Moreover, y^+ lower peaks corresponds to wall shear stress higher peaks and wall shear stress overestimation.

CONCLUSIONS

In this paper fully developed single-phase turbulent flow inside helically coiled pipes was addressed. New single-phase friction pressure drops data were collected at SIET labs, in a test facility simulating the SG of an integral SMR reactor of Generation III+. Predictions from some of the most common friction factor correlations available in literature were compared to experimental data, in particular Ito, White and Mishra and Gupta correlations. Also more data available in literature have been considered for comparison. Ito and Mishra and Gupta correlations showed very good agreement with the experimental measurements, with average errors always under 5% in the fully developed turbulent region.

Experimental friction factors were then used to test different turbulence models with the CFD commercial code FLUENT, to assess their capability to predict the friction factor coefficient and the wall shear stress in helically coiled channels.

In particular standard, RNG and realizable *k-ε* models, SST *k-ω* model and RSM were considered. The near wall region was treated with the standard wall function, the non-equilibrium wall function and with the enhanced wall treatment implemented in FLUENT, which resolves the near wall region all the way to the wall. As long as the wall functions are considered, *k-ε* models and RSM provide satisfactory results for medium-high Reynolds numbers. In particular, for $Re > 20000$, errors between calculated friction factor coefficients and experimental data are always below the 10%, comparable although slightly higher with respect to the Ito correlation. The best results are given by the realizable *k-ε* model with the standard wall function, which appears reliable also in the region $15000 < Re < 20000$. As concerns the RSM, the major complexity and computational cost introduced by the model are not balanced by a significant improvement in the computation results.

At low-medium Reynolds numbers, all the models overestimate the friction factor coefficient. Transition region and low Reynolds number region are critical for turbulence model, in particular when the wall function approach is considered. Furthermore, when helical geometry is addressed, the value of y^+ varies along the circumference of the pipe for the asymmetrical shape of the velocity profile and the presence of the secondary motion. A preliminary analysis showed

lower peaks of y^+ ending in the viscous sub-layer that correspond to overestimated peaks of the wall shear stress, not observable when the near wall region is resolved. More studies are needed on the subject, and more work could be foreseen to improve the wall function performances in helical geometry.

A remarkable improvement of the results was observed solving the near wall region all the way to the wall, using a finer grid. Predictions are satisfactory for all the range of Reynolds numbers. Also in this case, the best results are provided by the realizable k-ε model, which shows deviations from experimental data comparable or even better with respect to the Ito correlation.

Nomenclature

D	coil diameter [m]
d	pipe diameter [m]
De	Dean number [-]
f_D	Darcy friction factor coefficient [-]
I	turbulence intensity [%]
K	Karman constant
k	turbulent kinetic energy [m^2/s^2]
k_0	inlet turbulent kinetic energy [m^2/s^2]
L	turbulence characteristic length scale [m]
p	pressure [Pa]
Re	Reynolds number [-]
u	velocity [m/s]
u^*	dimensionless velocity [-]
u_0	inlet velocity [m/s]
y^+	dimensionless distance from the wall [-]
β_0	torsion parameter [-]
δ	dimensionless coil curvature [-]
ε	dissipation rate of turbulent kinetic energy [m^2/s^3]
ε_0	inlet dissipation rate of turbulent kinetic energy [m^2/s^3]
ρ	density [kg/m^3]
τ	dimensionless coil torsion [-]
ω	specific dissipation rate [1/s]

References

[1] Carelli, M. D., Conway, L. E., Oriani, L., Petrovic, B., Lombardi, C. V., Ricotti, M. E., Barroso, A. C. O., Collado, J. M., Cinotti, L., Todreas, N. E., Grgic, D., Moraes, M. M., Boroughs, R. D., Ninokata, H., Ingersoll, D. T., Oriolo, F., 2004, "The Design and the Safety Features of the IRIS Reactor", Nuclear Engineering and Design, **230**, pp. 151-167.

[2] Berger, S. A., Talbot, L., Yao, L. S., 1983, "Flow in Curved Pipes", Annual Review of Fluid Mechanics, **15**, pp. 461-512.

[3] Shah, R. K., and Joshi, S. D., 1987, "Convective Heat Transfer in Curved Ducts", *Handbook of Single-Phase Convective Heat Transfer*, S. Kakac, R. K. Shah, W. Hung "Eds.", Wiley Interscience, New York.

[4] Naphon, P., and Wongwises, S., 2006, "A Review of Flow and Heat Transfer Characteristics in Curved Tubes", Renewable and Sustainable Energy Reviews, **10**, pp. 463-490.

[5] Dean, W. R., 1927, "Note on the Motion of Fluid in a Curved Pipe", Philosopical Magazine, 4(20), pp. 208-223.

[6] Adler, M., 1934, "Strömung in Gekrümmten Rohren", Zeitschrift für Angewandte Mathematik und Mechanik, **14**, pp. 257-275.

[7] Seban, R. A., and McLaughlin, E. F., 1963, "Heat Transfer in Tube Coils with Laminar and Turbulent Flow", International Journal of Heat and Mass Transfer, **6**, pp. 387-395.

[8] Yamamoto, K., Akita, T., Ikeuchi, H., Kita, J., 1995, "Experimental Study of the Flow in a Helical Circular Tube", Fluid Dynamics Research, **16**, pp. 237-249.

[9] White, C. M., 1932, "Fluid Friction and its Relation to Heat Transfer", Transactions of the Institute of Chemical Engineering, **10**, pp. 66-86.

[10] Ito, H., 1959, "Friction Factors for Turbulent Flow in Curved Pipes", Transaction of the ASME D, Journal of Basic Engineering, **81**, pp. 123-124.

[11] Mishra P., and Gupta, S. N., 1979, "Momentum Transfer in Curved Pipes 1. Newtonian Fluids; 2. Non-Newtonian Fluids.", Industrial and Engineering Chemistry Process Design and Development, **18**, pp. 130-142.

[12] Ali, S., 2001, "Pressure Drop Correlations for Flow through Regular Helical Coil Tubes", Fluid Dynamic Research, **28**, pp. 295-310.

[13] Yang, G., and Ebadian, M. A., 1996, "Turbulent Forced Convection in a Helicoidal Pipe with Substantial Pitch", International Journal of Heat and Mass Transfer, **39**(10), pp. 2015-2022.

[14] Lin, C. X., and Ebadian, M. A., 1997, "Developing Turbulent Convective Heat Transfer in Helical Pipes", International Journal of Heat and Mass Transfer, **40**(16), pp. 3861-3873.

[15] Lin, X. C., and Ebadian, M. A., 1999, "The Effects of Inlet Turbulence on the Development of Fluid Flow and Heat Transfer in a Helically Coiled Pipe", International Journal of Heat and Mass Transfer, **42**, pp. 739-751.

[16] Li, L. J., Lin, C. X., Ebadian, M. A., 1998, "Turbulent Mixed Convective Heat Transfer in the Entrance Region of a Curved Pipe with Uniform Wall-Temperature", International Journal of Heat and Mass Transfer, **41**, 3793-3805.

[17] Kumar, V., Saini, S., Sharma, M., Nigam, K. D. P., 2006, "Pressure Drop and Heat Transfer Study in Tube-in-Tube Helical Heat Exchanger", Chemical Engineering Science, **61**, pp. 4403-4416.

[18] Jayakumar, J. S., Mahajani, S. M., Mandal, J. C., Vijayan, P. K., Bhoi, R., 2008, "Experimental and CFD Estimation of Heat Transfer in Helically Coiled Heat Exchangers", Chemical Engineering Research and Design, **86**, pp. 221-232.

[19] Jayakumar, J. S., Mahajani, S. M., Mandal, J. C., Iyer, K. N., Vijayan, P. K., 2010, "CFD Analysis of Single-Phase Flows Inside Helically Coiled Tubes", Computers and Chemical Engineering, **34**, pp. 430-446.

[20] FLUENT, 2004, *FLUENT User's Guide, Release 6.2*, FLUENT Inc., Lebanon, NH.

[21] Cincolini, A., and Santini, L., 2006, "An Experimental Investigation Regarding the Laminar to Turbulent Flow Transition in Helically Coiled Pipes", Experimental Thermal and Fluid Science, **30**, pp. 367-380.

[22] Papini, D., Colombo, M., Cammi, A., Ricotti, M. E., Colorado, D., Greco, M., Tortora, G., 2011, "Experimental Characterization of Two-Phase Flow Instability Thresholds in Helically Coiled Parallel Channels", *Proc. of the International Congress on Advances in Nuclear Power Plants*, Nice, France.

[23] Launder, B. E., and Spalding, D. B., 1972, "The numerical Computation of Turbulent Flows", Computer Methods in Applied Mechanics and Engineering, **3**, pp. 269-289.

[24] Yakhot, A., and Orszag, S. A., 1986, "Renormalization Group Analysis of Turbulence. I. Basic Theory", Journal of Scientific Computing, **1(1)**, pp. 1-51.

[25] Choudhury, D., 1993, "Introduction to the Renormalization Group Method and Turbulence Modeling", Technical Memorandum TM-107, Fluent Inc.

[26] Shih, T. H., Liou, W. W., Shabbir, A., Zhu, J., 1995, "A New k-ε Eddy-Viscosity Model for High Reynolds Number Turbulent Flows – Model Development and Validation", Computer Fluids, **24**(3), pp. 227-238.

[27] Menter, F. R., 1994, "Two-Equation Eddy-Viscosity Turbulence Models for Engineering Applications", J 32, American Institute of Aeronautics and Astornautics.

[28] Launder, B.E., Reece, G. J., Rodi, W., 1975, "Progress in the Development of a Reynolds-Stress Turbulence Closure", Journal of Fluid Mechanics, **68**(3), pp. 537-566.

[29] Launder, B. E., 1989, "Second-Moment Closure: Present… and Future?", International Journal of Heat and Fluid Flow, **10**(4), pp. 282-300.

[30] Kim, S. E., Choudhury, 1995, "A Near-Wall Treatment Using Wall Functions Sensitized to Pressure Gradient", *Separated and Complex Flows*, ASME.

PART III

SUPERPOSITION OF DWOs WITH LEDINEGG-TYPE INSTABILITIES

This section describes the superposition of DWO type instability with Ledinegg type instability. Ledinegg flow excursions were observed during test runs at the lowest pressure level (P = 20 bar), the highest mass flux (G = 600 kg/m^{2}s), and high inlet subcooling values (x_{in} < -15%). Ledinegg type instabilities (ref. Ledinegg) occur when a heated channel operates in the negative slope region of the pressure drop versus flow rate curve (channel characteristics). In this respect, the boundary condition of constant-pressure-drop given by parallel channels acts as a flat pump external characteristics, forcing each channel into a wide flow excursion up to the reaching of new operating points on the internal characteristics. For the case of two parallel channels, such Ledinegg instability mechanism is illustrated qualitatively in Fig.13.

Fig.14 shows the flow rate evolution in each channel in presence of a Ledinegg type instability (system parameters: P = 24 bar, G = 601 kg/m^{2}s, T_{in} = 134 °C, Q = 46.5 kW). Flow excursion is evident, as Channel A flow rate increases. On the contrary, flow rate in Channel B reduces proportionally to preserve the imposed total mass flow rate. Constant total pressure drop condition is respected across the two tubes. Ledinegg instability occurrence showed to be critical since an anticipated DWO onset was recorded in the channel with lower flow rate (Channel B in this case), following small increases of the supplied thermal power. Besides, further increases of thermal power permitted firstly to damp the flow excursion and finally to trigger fully developed DWOs (the corresponding instability threshold is reported as the point of highest N_{sub} in the stability map at G = 600 kg/m^{2}s).

The mentioned behaviour is even more evident considering the Ledinegg transient described in Fig.15, referring to higher inlet subcooling (T_{in} = 122 °C), where superimposition with DWOs is clearly depicted. Initial flow excursion (Fig.15-(a)) leads to an increase of Channel A flow rate and decrease of Channel B flow rate (as above). The drop in Channel B flow rate is indeed such to yield anticipated DWO inception (with a supplied electrical power of 65 kW). The instability triggered in Channel B causes Channel A flow rate to oscillate as well (Fig.15-(b)). That is, for the considered parallel channel system, the instability is reached in one sole channel that induces then the other (ref. Guo, Yadi, Papini2012). An increase of thermal power is sufficient to switch off the flow excursion, and – via the consequent increase of Channel B flow rate – to damp out the DWOs (Fig.15-(c)). At a power level of 90 kW (gross electrical power) the system is completely stable (Fig.15-(d)). Finally, a further increase of thermal power causes fully developed DWOs to occur. At the end, it is just noticed that the described transient with superimposition between Ledinegg and DWO instability occurs exactly in the "nose" region (at high inlet subcooling) of the stability map in the N_{pch}–N_{sub} plane (ref. Ambrosini, Papini2012), which is currently under characterization by means of new dedicated experimental runs (ref. ICAPP2012).

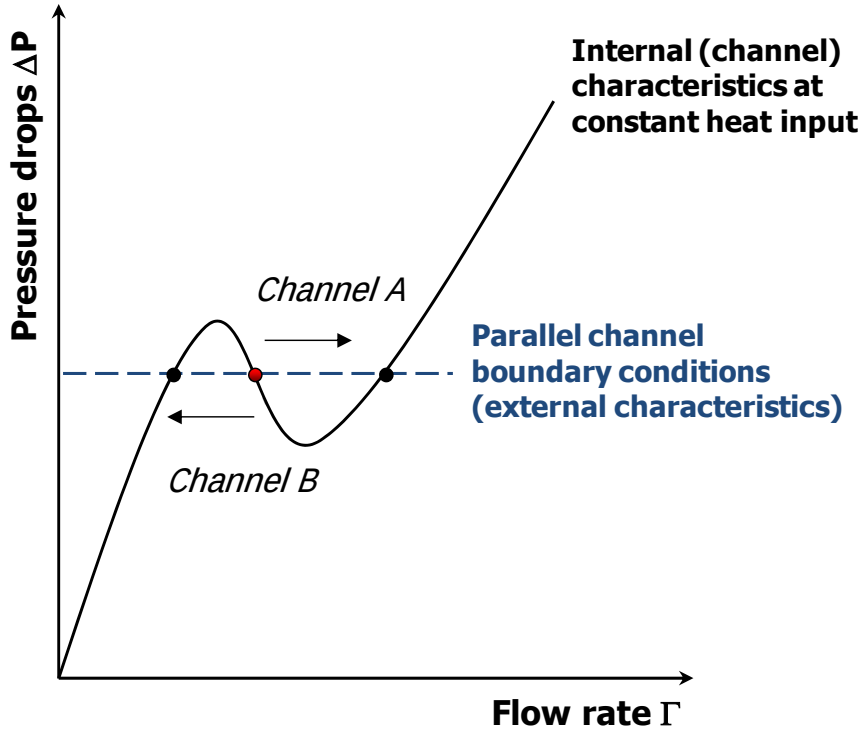

Fig. 13. Sketch of Ledinegg instability mechanism under parallel channel boundary conditions.

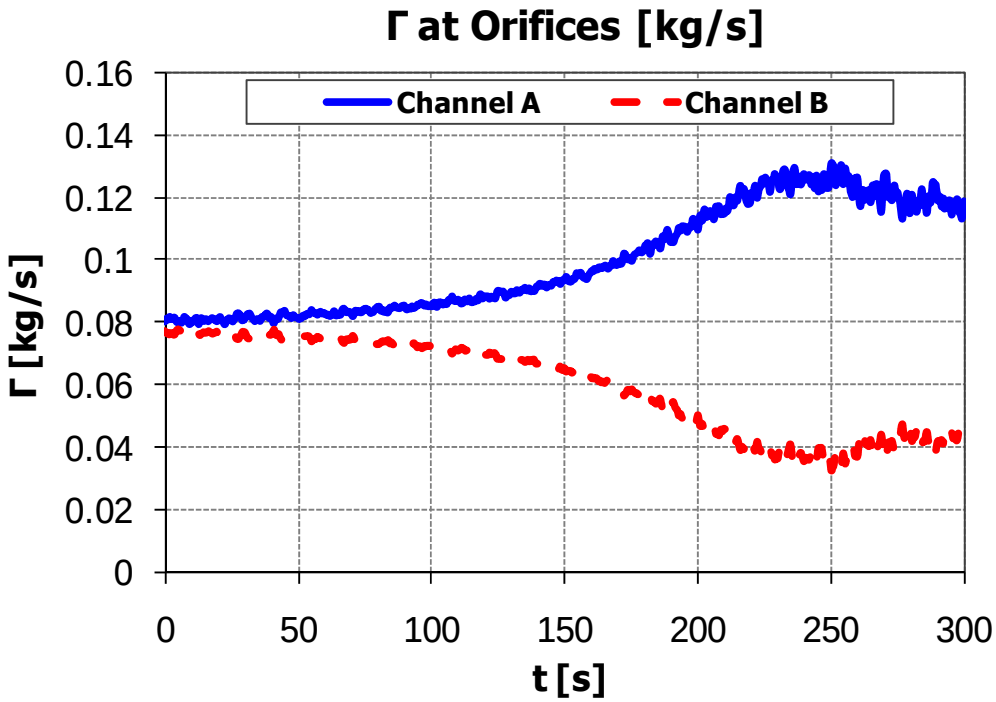

Fig. 14. Flow rate recorded in the two channels during a Ledinegg transient.

Data collected with: P = 24 bar; T_{in} = 134 °C; G = 601 kg/m^{2}s. Transient to Q = 50 kW (gross electrical power supplied per tube).

(a)

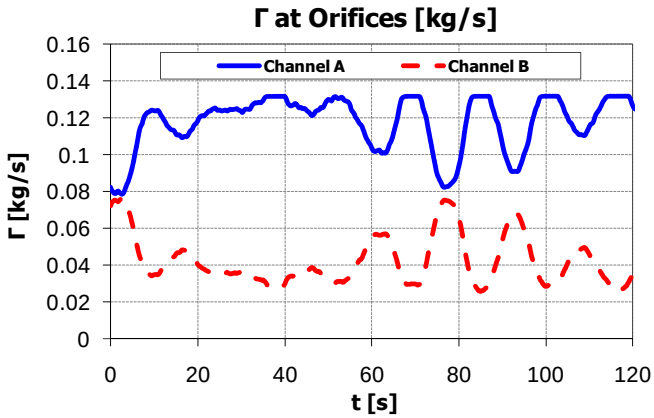
Γ at Orifices [kg/s]
Channel A
Channel B
Γ [kg/s]
t [s]
0.16
0.14
0.12
0.1
0.08
0.06
0.04
0.02
0
0
20
40
60
80
100
120

(b)

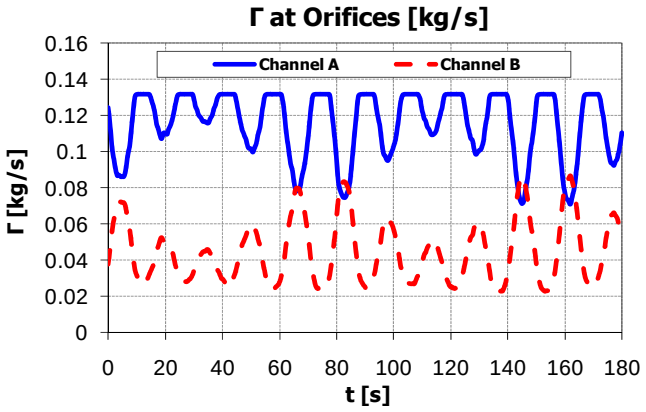
Γ at Orifices [kg/s]
Channel A
Channel B
Γ [kg/s]
t [s]
0.16
0.14
0.12
0.1
0.08
0.06
0.04
0.02
0
0
20
40
60
80
100
120
140
160
180

(c)

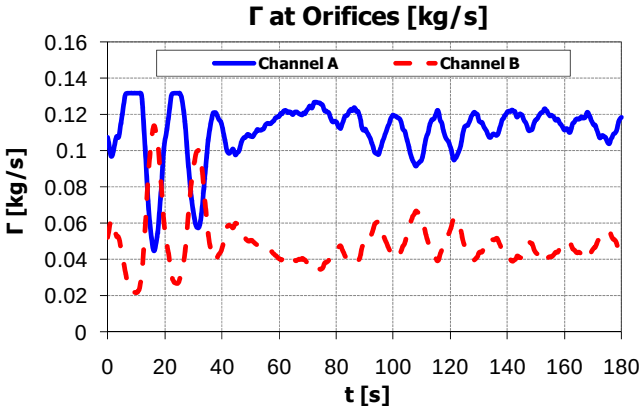
Γ at Orifices [kg/s]
Channel A
Channel B
Γ [kg/s]
t [s]
0.16
0.14
0.12
0.1
0.08
0.06
0.04
0.02
0
0
20
40
60
80
100
120
140
160
180

(d)

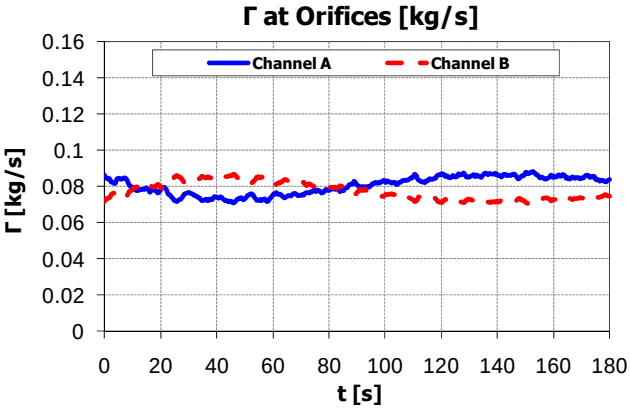
Γ at Orifices [kg/s]
Channel A
Channel B
Γ [kg/s]
t [s]
0.16
0.14
0.12
0.1
0.08
0.06
0.04
0.02
0
0
20
40
60
80
100
120
140
160
180

(e)

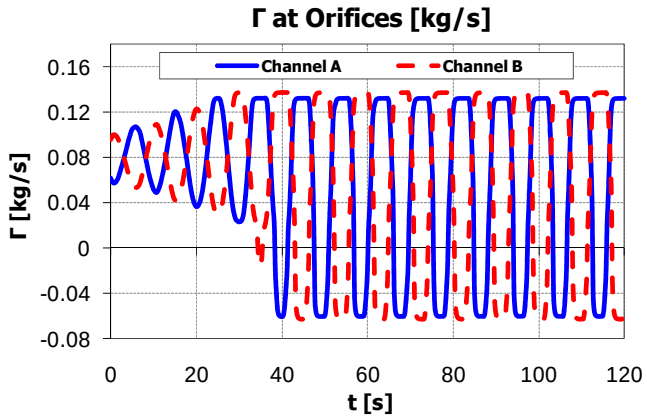

Fig. 15. Flow rate transients during superimposition of Ledinegg type instabilities with density wave oscillations. Data collected with: P = 21 bar; T_{in} = 122 °C; G = 603 kg/m^{2}s. Gross electrical power supplied per tube: (a) 65 kW – (b) 65 kW – (c) 75 kW – (d) 90 kW – (e) 96 kW.

THEORETICAL ANALYSIS OF THE RESULTS

Simplified analytical models are useful to study basic thermal-hydraulic phenomena. In order to grasp the fundamental features of DWO mode and predict the instability threshold dependence on the main system parameters, a theoretical lumped parameter model – moving boundary kind (ref., multiple) – has been proposed (Papini et al., 2012). The model of Papini et. al (2012), based on the integration of mass, energy and momentum one-dimensional equations, was built in time domain; steady-state conditions were perturbed with small stepwise changes of some operating parameters simulating an actual transient, such as power increase in the real system. The stability threshold was reached when undamped or diverging oscillations were induced. Homogeneous two-phase flow model was assumed within the boiling region. Such model was tested dealing with the simplified vertical tube geometry, also owing to the availability of similar works in the open literature for validation purposes (Ambrosini, Munoz, Rizwan).

Secondary objective of this paper is to apply the modelling tools developed for DWO instability prediction to the simulation of the peculiar results obtained with the experimental campaign.

Refinement of the analytical model

Parallel channel configuration of the analytical model is considered (Papini et al., 2012). Geometrical and operational conditions of the experimental facility at SIET labs are reproduced.

Main modifications to the model dynamic coefficients include the introduction of a riser section downstream the heated section (destabilizing on parallel channel behaviour) and the approximation of the helical shape by assuming a straight channel long as the helical tube and with the same inclination of the helix. This hypothesis permits to calculate properly both, tube frictional pressure drops (function of tube length) and gravitational pressure drops (dependent on geodetic elevation $h(z) = z \sin\theta$). The modelling approach is depicted in Fig.16.

The presence of a riser unheated section, given by the final 8 m of test section tubes where no thermal power is provided, is accounted for by introducing the respective pressure drop terms within the momentum balance equation (see (Papini et al., 2012) for details). The exit quality value $x_{ex}(t)$, which is one of the model state variables, and the

respective void fraction value $\alpha_{ex}(t)$ must be considered for calculating frictional and gravitational pressure drops in the riser portion of each of the two channels. No accelerative pressure drops are introduced by the riser (no phase change occurs). The two terms (gravitational and frictional, respectively) introduced to simulate the effects of the riser are listed below:

$$\Delta P_{grav}^{R} = g \sin\theta (1-\alpha_{ex})\rho_f H_R + g \sin\theta \alpha_{ex} \rho_g H_R \tag{5}$$

$$\Delta P_{fricl}^{R} = f \frac{H_R}{d} \Phi_{ex}^2 \frac{G_{ex}^2}{2\rho_f} \tag{6}$$

Specific empirical correlations are considered to represent the flow structure, and in particular the frictional pressure drops inside a helically coiled tube. As concerns single-phase frictions, the friction factor f (Darcy kind) is evaluated with White correlation (Guo et al., 2001) for laminar regime, and Ito (Ito, 1959) and Ruffell (Ruffell, 1974) correlations for turbulent regime. Respectively:

$$\frac{f}{f_s} = \frac{1}{1-\left[1-\left[\frac{11.6}{\mathrm{Re}(d/D)^{0.5}}\right]^{0.45}\right]^{\frac{1}{0.45}}} \qquad \textit{White correlation} \tag{7}$$

where $f_s = 64/\mathrm{Re}$ is the friction factor for straight tubes (laminar regime). Transition from laminar flow to turbulent flow is governed by the critical Reynolds number suggested by Ito (Guo et al., 2001):

$$\mathrm{Re}_{cr} = 20000\left(\frac{d}{D}\right)^{0.32} \tag{8}$$

Ito correlation is used for its high accuracy in turbulent regime, as long as $\mathrm{Re} \le 10^5$. For higher Reynolds number (typical of vapour phase), Ruffell correlation is recommended (valid for $5\cdot10^3 \le \mathrm{Re} \le 6\cdot10^5$):

$$f = 0.304\,\mathrm{Re}^{-0.25} + 0.029\left(\frac{d}{D}\right)^{0.5} \qquad \text{if } \mathrm{Re}_{cr} \le \mathrm{Re} \le 10^5 \qquad \textit{Ito correlation} \tag{9}$$

$$f = 0.015 + 2.53\left(\frac{d}{D}\right)^{0.275} \mathrm{Re}^{-0.4} \qquad \text{if } \mathrm{Re} \ge 10^5 \qquad \textit{Ruffell correlation} \tag{10}$$

The present model does not consider subcooled boiling, dryout and post-dryout regions.

It is just mentioned that the void fraction (generally evaluated from empirical information for complex systems) is – within the present model – set by homogeneous flow model assumption. This simplification, fundamental to get the analytical integration of the governing equations in the two-phase zone, might considerably affect the predictions on the helical-coiled system under analysis.

Two-phase friction factor multiplier formula

Analytical calculations of DWO instability are strongly influenced by the considered two-phase frictional model (ref. Furutera, Goswami, Nayak, Papini). Proper representation of the stationary pressure drop distribution within the analysed system is in fact fundamental to obtain, with transient calculations, an accurate prediction of the instability threshold.

On this basis, a suitable expression for the two-phase friction factor multiplier was tuned on the steady-state characteristics of the helical coil system (Colorado et al., 2011) and implemented within the analytical model for DWO study. In particular, it was chosen to tune the widespread and sound Lockart-Martinelli multiplier approach (ref.?), as done also by other authors on the basis of their experimental findings (ref., Xi, Torino, anche Cionco ?). The modified Lochkart-Martinelli multiplier (only-liquid kind) used for the calculations reads (Colorado et al., 2011):

$$\Phi_l^2 = 1 + \frac{3.2789}{X_{tt}} + \frac{0.3700}{X_{tt}^{2.0822}} \tag{11}$$

To comply with the form of the modelling equations, passing from "only-liquid" to "liquid-only" mode is required. The following relation (ref. Todreas) is considered:

$$\Phi_{lo}^2 = \Phi_l^2 (1-x)^{1.75} \tag{12}$$

The instability predictions obtained following Eq.(11) have been assessed by considering specific test-case conditions (P = 40 bar, G = 300 kg/m^{2}s, k_{in} = 20, k_{ex} = 0). Fig.17 provides the theoretical comparison with several two-phase multiplier models, rigorously valid however for straight tubes (excepted Guo correlation (ref.)). As discussed in (Papini et. al, 2012), the higher are the two-phase friction pressure drops calculated by the considered model, the more unstable is the system. In this case, the parallel channel system is most unstable (smallest stability region) considering Guo correlation. Follow in this order: Jones, Lockhart-Martinelli (L-M) and Friedel models (almost overlapped); homogeneous model; modified Lockhart-Martinelli, i.e. Eq.(11). While all the multiplier formulas referring to straight geometry depict a typical "L shape" stability boundary (ref. Papini capitol), both models referring to helical geometry (Guo and modified L-M) deviate from classical shape towards a "straighter" boundary (more close to a line of constant equilibrium quality). The stabilizing effect given by reducing the subcooling near the saturation is not evident.

At the end, it is pointed out that the steady-state pressure drops calculated by Eq.(11), tuned on the real behaviour of the facility (Colorado et al.), are lower even than HEM friction predictions. Hereby, this helical tube system is predicted to be more stable than conventional vertical tube systems. This can be induced by the peculiar flow pattern that might be established owing to the small inclination angle and the nearly horizontal features of the helical coil.

Theoretical results and discussion

The modified L-M friction multiplier, in the form given by Eq.(11), has been applied to simulate the experimental campaign matrix. The results are shown in Fig.18. Just one flow rate value (i.e., G = 400 kg/m^{2}s) has been considered at 80 bar, where however less threshold points have been collected. "Basically open" inlet valve configuration (k_{in} = 45) has been referenced for all the calculations.

New findings are hereby pointed out. Mass flow rate influence on the stability boundary is introduced, as the system looks more stable at the lowest mass flux (G = 200 kg/m^{2}s). If one considers carefully the experimental stability maps, this feature is not excluded at all. Moreover, whereas at medium-high flow rates (G = 400 kg/m^{2}s and G = 600 kg/m^{2}s) the stability boundary still agrees with the classical "L shape" of vertical tube geometry (ref. Papini 2012), the peculiar behaviour of this helical-coiled system is properly caught at G = 200 kg/m^{2}s. Beyond the "conventional" trend at medium-high subcoolings (iso-quality stability boundary followed by slight stabilization), the "non-conventional" destabilizing feature at low subcoolings is apparent. Also the stabilizing effect of a pressure level increase is well reproduced.

At the end, the calculated periods of DWO oscillations are discussed. Fig.19 shows the period-over-transit time ratio predicted for each condition of the test matrix. Fluid transit time is again calculated according to classical homogeneous flow theory, as in Eq.(4). The drop of $T/\square$ at low inlet subcooling (N_{sub} < 2) is ascribed to the lumped-parameter characteristics of the analytical model (working with two sole nodes, less accurate predictions are obtained when the two-phase region becomes too large) (ref. Papini 2012). Nevertheless, a very interesting feature must be highlighted. Considering the curves at the lowest mass flux (G = 200 kg/m^{2}s) – red and black curves – an exact prediction of the experimental oscillation period is depicted: DWO period results in fact rather small when compared to the mixture transit time ($T/\square$ of about 0.5), which is in agreement with the experimental findings. That is, when the instability behaviour of the investigated system seems to be properly represented (i.e., at low mass flux), hence the frictional characteristics of the test section, all the collected theoretical results are consistent also in terms of period of the oscillations. It is remembered that, as observed by Rizwan-Uddin (1994), it is the pressure drop fractional distribution within the heated channel that influences the instability onset and affects the respective oscillations period. The period is "high" with more delayed feedback effects (in case of major pressure drops concentrated near the outlet, that is with "high" two-phase friction), whereas the period is "low" with faster feedback effects (in case of major pressure drops concentrated near the inlet, that is with "low" two-phase friction). The latter is exactly the case of the helically coiled parallel tubes under analysis.

Comparison between theoretical and experimental results

Comparison between experimental threshold conditions and the respective predictions with the analytical lumped parameter model is addressed in the followings. For example, stability maps at the pressure of 40 bar and mass flux of 600 kg/m^{2}s are shown in Fig.20. Stability maps at the pressure of 40 bar and mass flux of 200 kg/m^{2}s are shown in Fig.21. Stability maps at the pressure of 80 bar and mass flux of 400 kg/m^{2}s are shown in Fig.22. The corresponding limit powers (at instability inception) are reported in Fig.23, Fig.24 and Fig.25 respectively.

The comparisons confirm what discussed in the previous sections. The analytical model of Papini et al. (2012), properly adapted to simulate the helical-coiled geometry, underestimates the instability threshold conditions (i.e., theoretically predicted instabilities occur at lower qualities). Moreover, whereas a qualitative agreement between predicted and experimental stability boundaries is not obtained at medium-high flow rate (G = 400 kg/m^{2}s and G = 600 kg/m^{2}s), rather satisfactory results turn out when the lowest flow rate value (G = 200 kg/m^{2}s) is considered. In these conditions, the peculiar stability boundary shape, experimentally found for the present system, is well predicted (Fig.21). Also the error in terms of threshold power prediction is lower (Fig.24). Finally, the comparison between model predictions and experimental findings is considerably better at high pressure (Fig.22; Fig.25), where the homogenous two-phase flow model – based on which the modelling equations have been integrated – is more accurate.

Such partial reproduction of the helical coil tube stability behaviour can be justified in light of some discussions about the experimental validation of the modified L-M equation – Eq.(11). Whereas its predictions on the pressure drops of the analysed helical-coiled tubes are basically exact with G = 200 kg/m^{2}s, a systematic error is introduced at higher flow rates (up to ~20% under diabatic conditions) (ref. Colorado), the error being such to overestimate two-phase frictional pressure drops (this is confirmed in our model by the anticipation of the instability onset). More details can be found in (Colorado et al., 2011) and in (Papini, thesis). Moreover, the difference between the homogenous model of void fraction (assumed within the theoretical calculations) and the "real" void fraction of the investigated helical tube plays to strengthen the described inaccuracies.

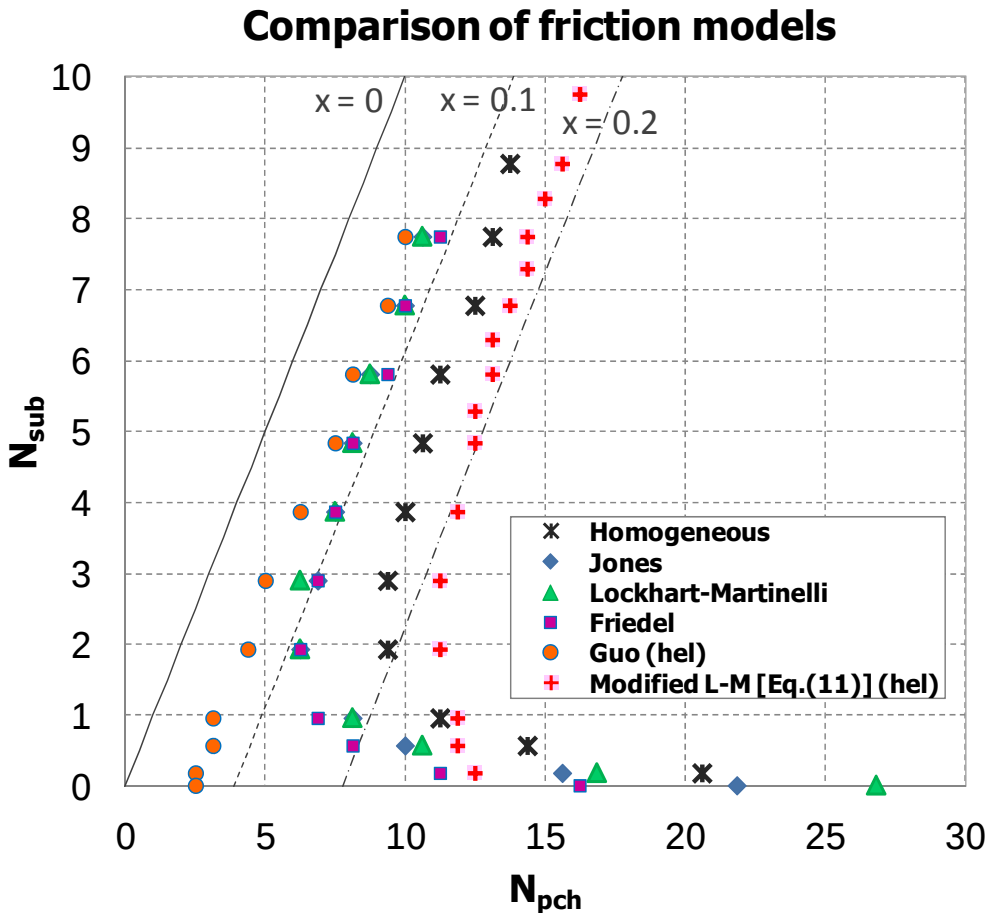

Fig. 17. Comparison of theoretical stability maps obtained with different two-phase multiplier models [P = 40 bar; G = 300 kg/m2s; kin = 20; kex = 0].

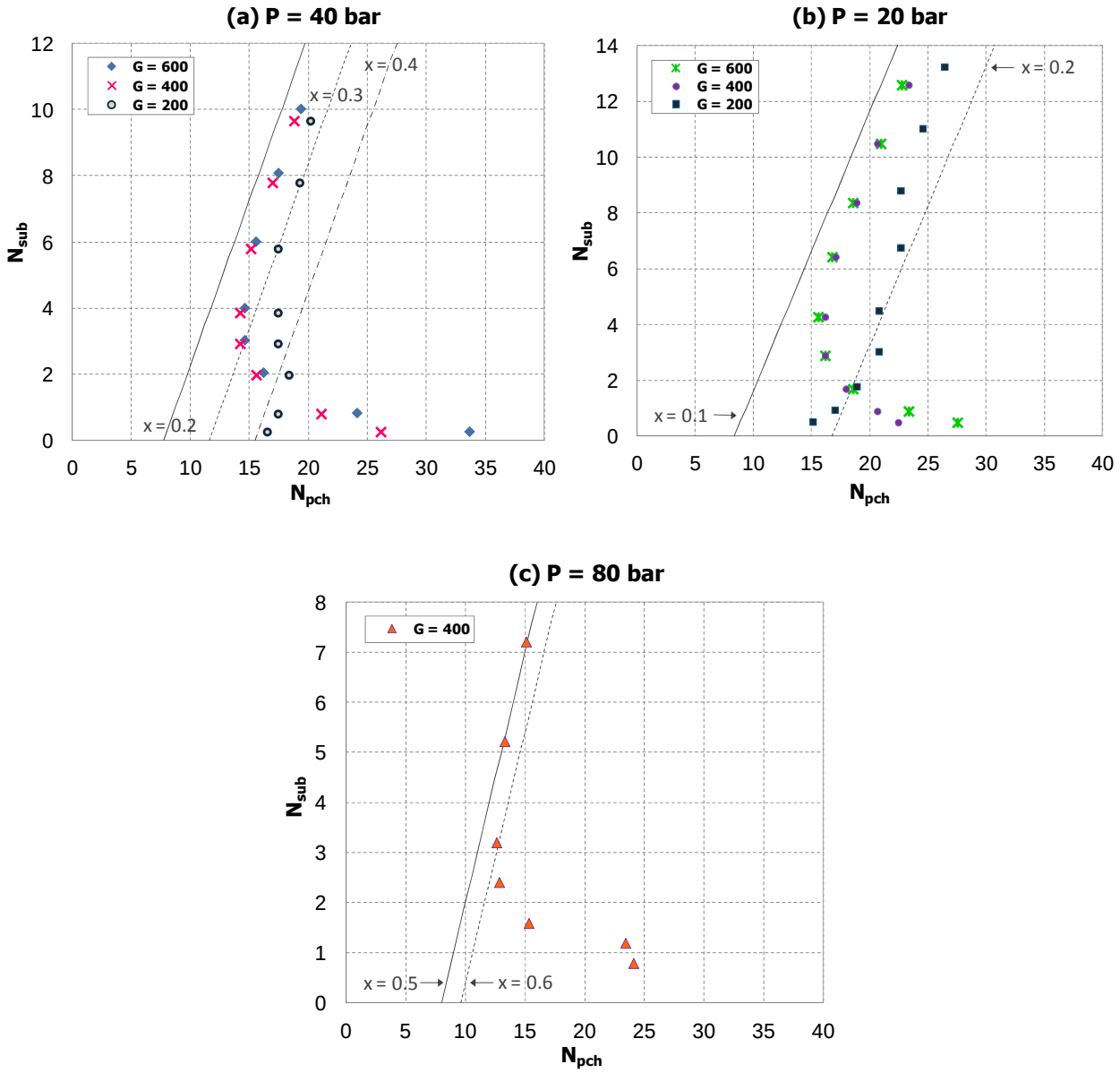

Fig. 18. Stability maps theoretically obtained according to modified Lockhart-Martinelli friction multiplier [Eq.(11)], at the pressures and mass fluxes of the experimental campaign.

(a) P = 40 bar – (b) P = 20 bar – (c) P = 80 bar

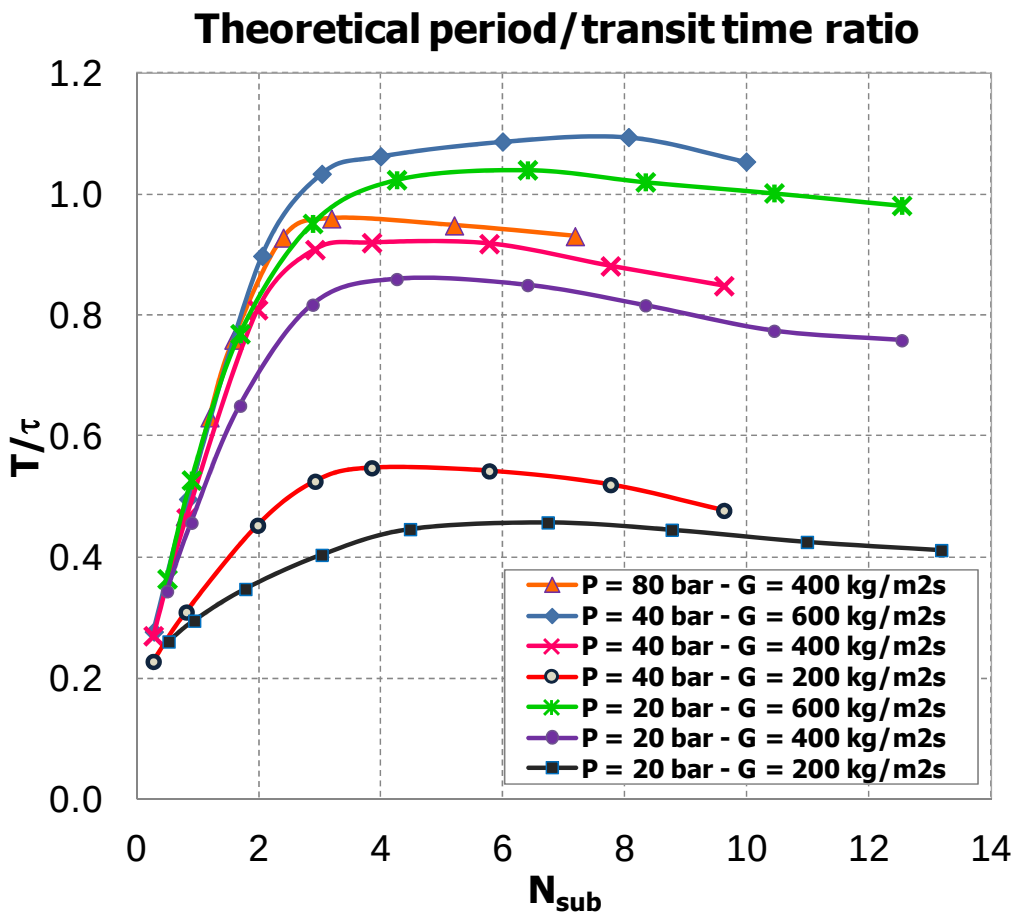

Fig. 19. Calculated period of oscillations to transit time ratio, as function of the subcooling number and at the pressures and mass fluxes of the experimental campaign [Friction model: modified Lockhart-Martinelli, Eq.(11)].

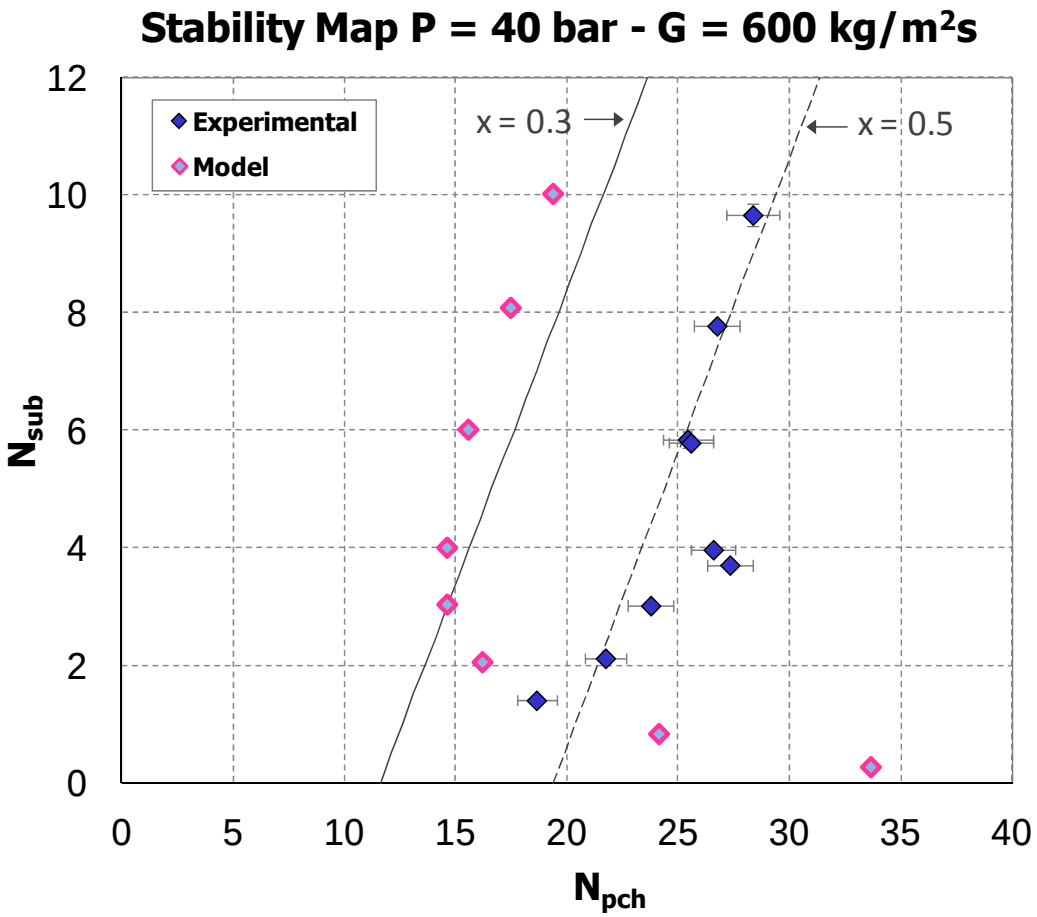

Fig. 20. Comparison between theoretical model and experiment in terms of stability map [P = 40 bar; G = 600 kg/m2s].

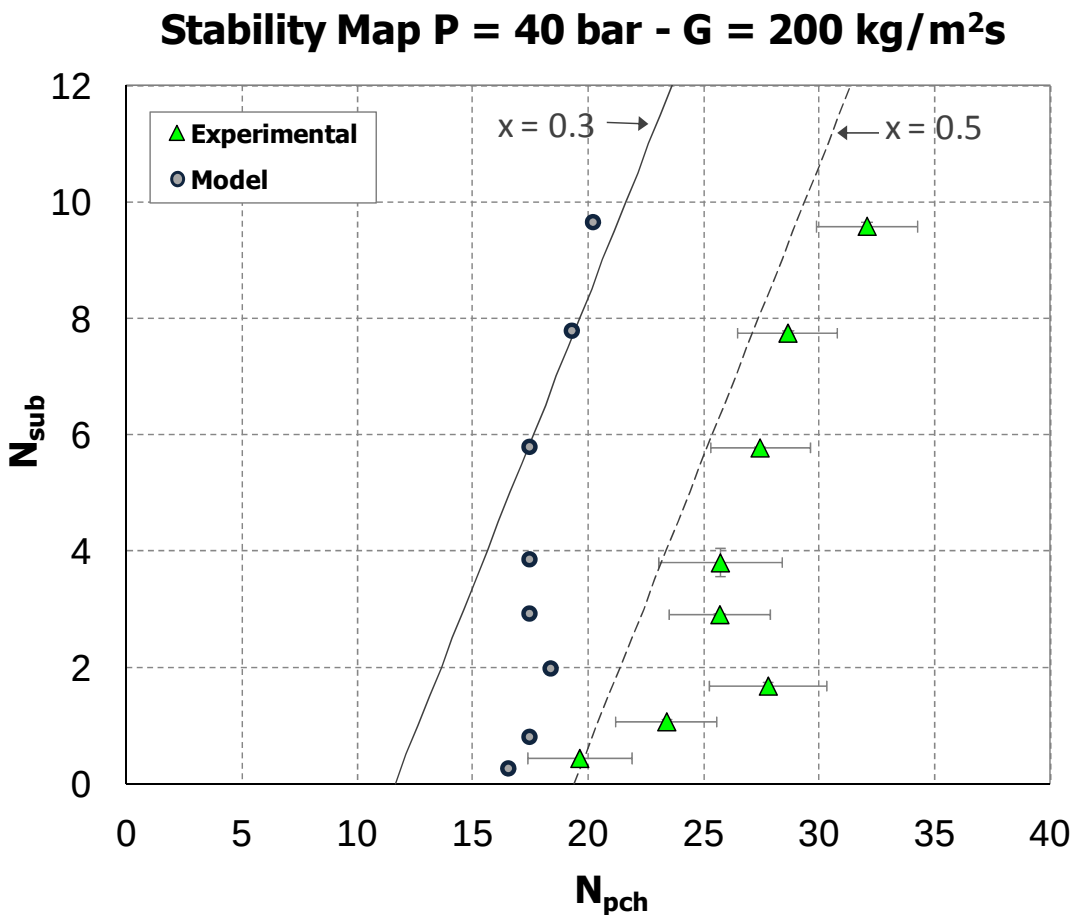

Fig. 21. Comparison between theoretical model and experiment in terms of stability map [P = 40 bar; G = 200 kg/m2s].

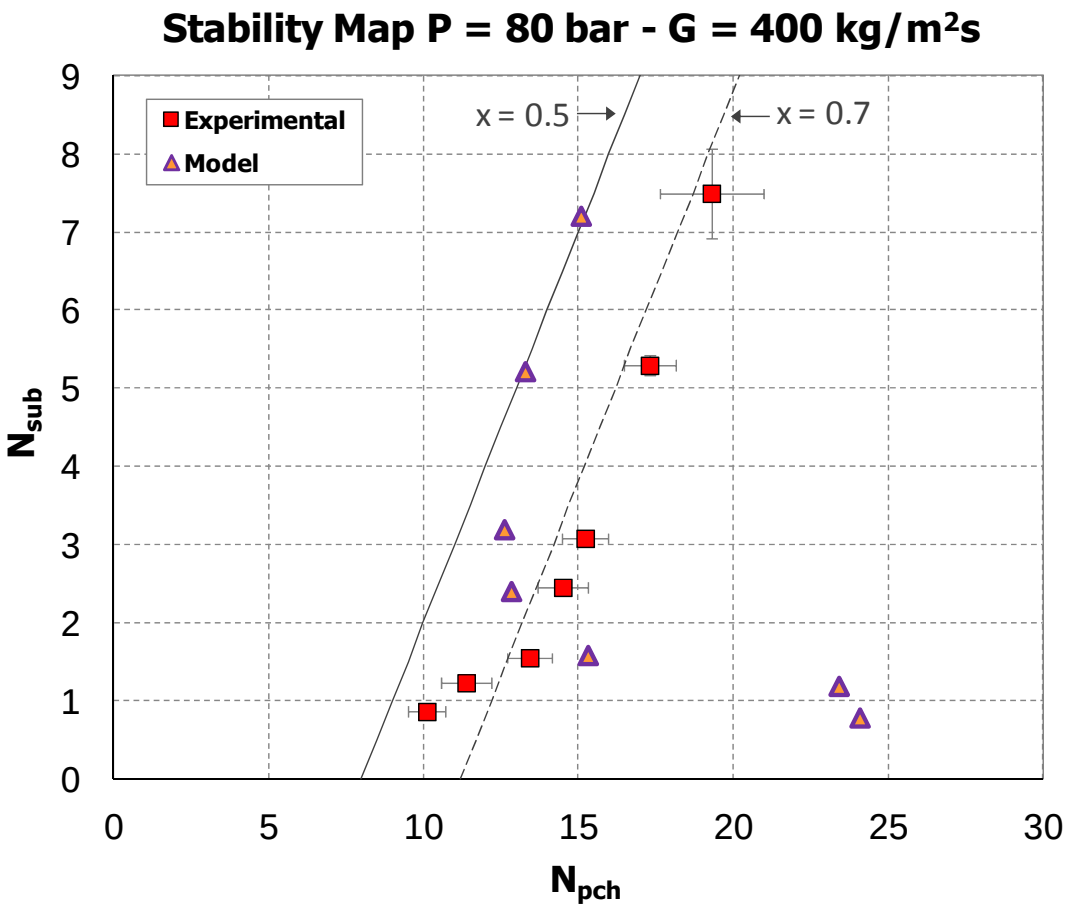

Fig. 22. Comparison between theoretical model and experiment in terms of stability map [P = 80 bar; G = 400 kg/m2s].

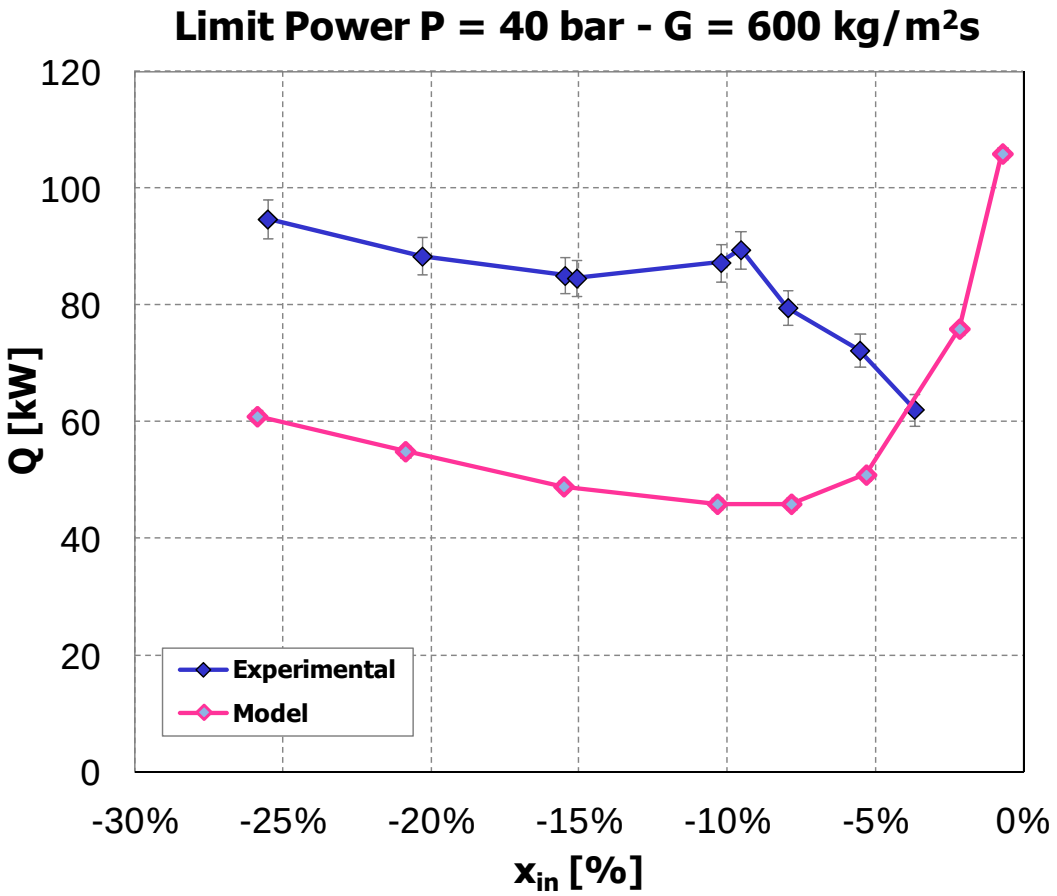

Fig. 23. Comparison between theoretical model and experiment in terms of limit power [P = 40 bar; G = 600 kg/m2s].

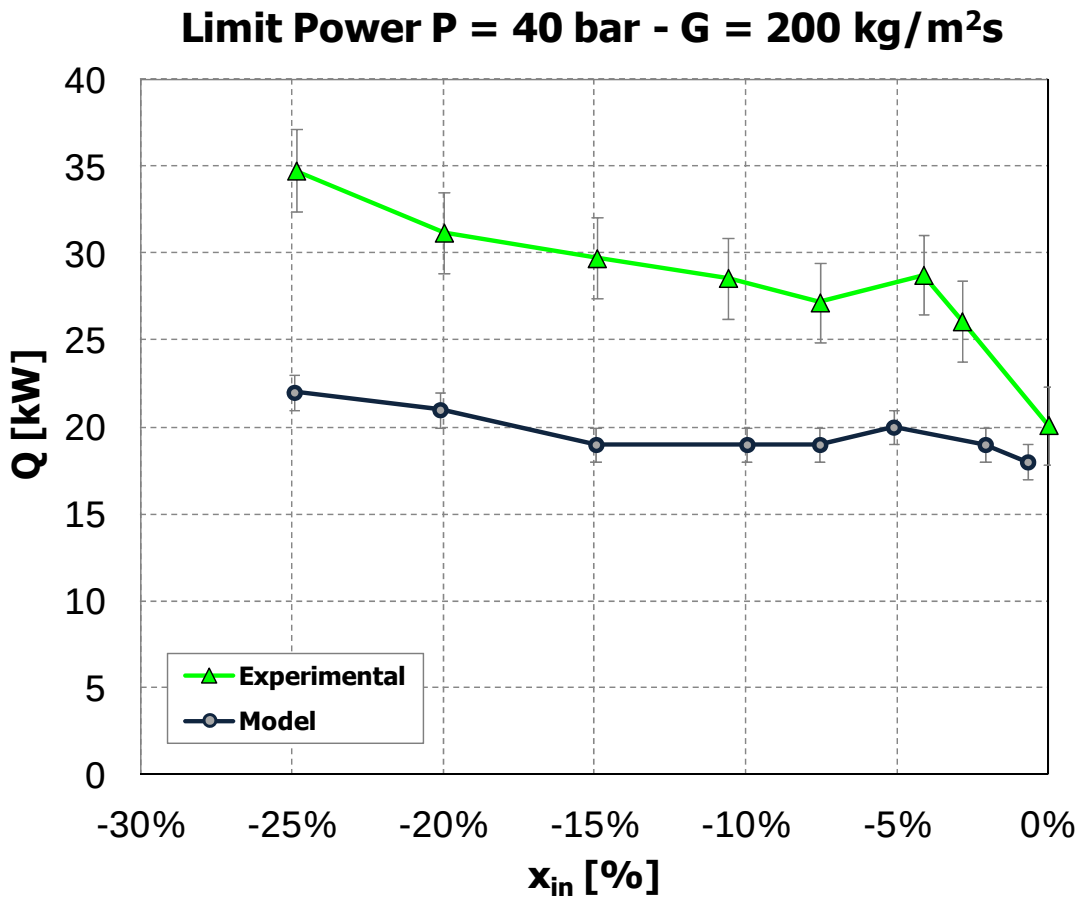

Fig. 24. Comparison between theoretical model and experiment in terms of limit power [P = 40 bar; G = 200 kg/m2s].

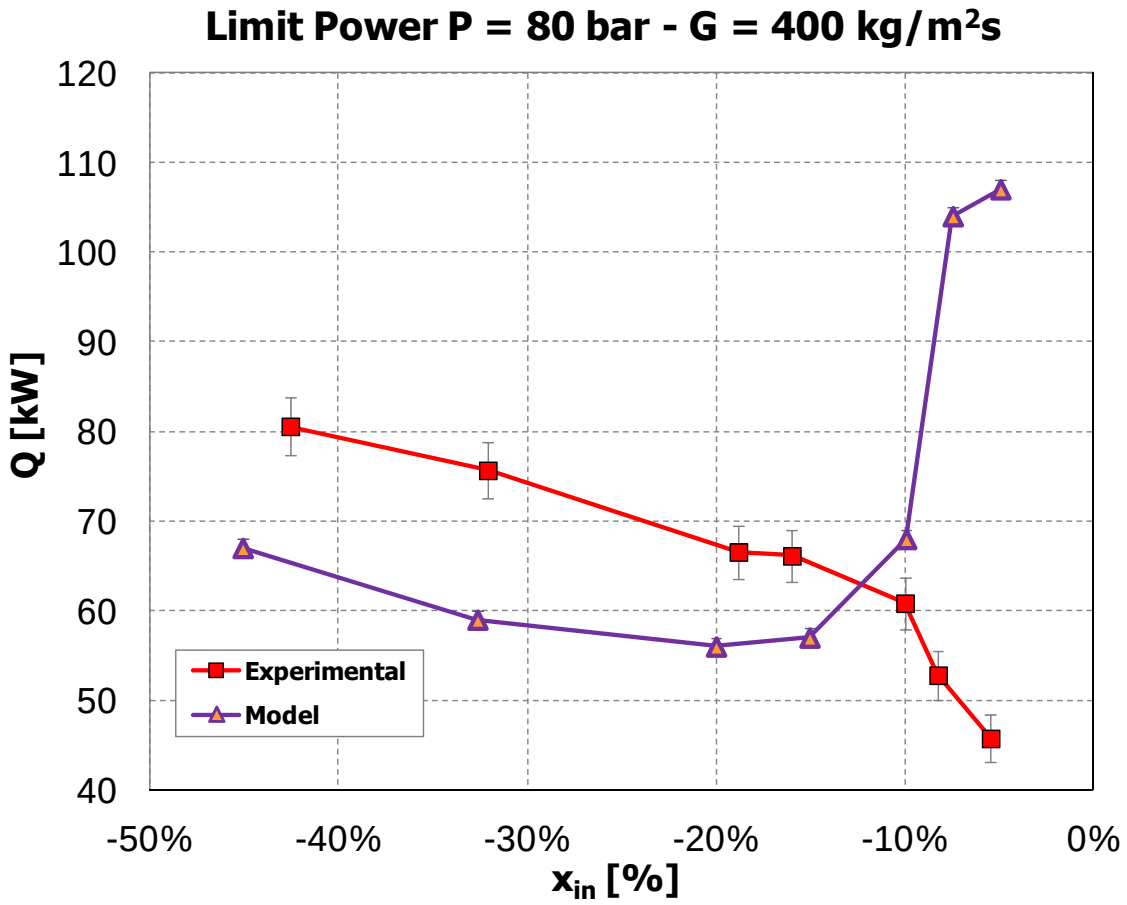

Fig. 25. Comparison between theoretical model and experiment in terms of limit power [P = 80 bar; G = 400 kg/m2s].

APPENDIX – EXPERIMENTAL DATABASE

The experimental campaigns performed within the 3rd year of activities (PAR II, MSE-ENEA), referred to:

1. single phase pressure drops (friction only) measurement in helical coil tubes;
2. adiabatic two-phase pressure drops;
3. density wave (DWO) instabilities;
4. TH system characterization of the helical coil tube (flow rate-pressure drops, Γ-Δp);
5. Ledinegg instabilities.

1. SINGLE-PHASE PRESSURE DROPS (friction only)

Δp_1, Δp_2, Δp_3 pressure drops refer to helical coil tube lengths $L_{1\ (DP3\text{-}4)}$= 3960 mm, $L_{2\ (DP4\text{-}5)}$= 3990 mm, $L_{3\ (DP7\text{-}8)}$= 3500 mm

T_{in} [°C]	p [bar]	Γ [kg/s]	Re	Δp_1 [kPa]	Δp_2 [kPa]	Δp_3 [kPa]
29.696	0.856	0.01424	1804	0.141	0.152	0.132
29.460	0.858	0.01496	1885	0.145	0.156	0.133
29.377	0.855	0.01495	1881	0.152	0.162	0.142
30.457	0.856	0.01638	2109	0.162	0.174	0.152
29.354	0.854	0.01631	2051	0.171	0.184	0.162
30.317	0.854	0.01802	2313	0.188	0.201	0.174
29.492	0.854	0.01799	2269	0.197	0.211	0.179
29.358	0.853	0.01947	2449	0.214	0.226	0.190
29.234	0.853	0.01946	2441	0.213	0.227	0.186
29.750	0.852	0.01999	2535	0.226	0.240	0.201
30.225	0.851	0.02082	2668	0.233	0.247	0.200
29.197	0.850	0.02234	2800	0.263	0.276	0.234
30.095	0.849	0.02317	2960	0.278	0.293	0.249
30.337	0.850	0.02335	2998	0.274	0.291	0.251
30.388	0.847	0.02518	3237	0.289	0.304	0.266
29.268	0.847	0.02542	3190	0.306	0.326	0.282
30.798	0.846	0.02649	3435	0.303	0.319	0.283
29.315	0.844	0.02818	3540	0.337	0.351	0.303
30.871	0.844	0.02929	3803	0.354	0.370	0.327
29.223	0.841	0.03080	3863	0.388	0.403	0.366
29.392	0.838	0.03305	4160	0.434	0.451	0.390
29.701	0.834	0.03680	4663	0.521	0.538	0.482
30.882	0.835	0.03683	4784	0.520	0.537	0.492

T_{in} [°C]	p [bar]	Γ [kg/s]	Re	Δp_1 [kPa]	Δp_2 [kPa]	Δp_3 [kPa]
29.911	0.831	0.03881	4939	0.568	0.588	0.524
30.142	0.825	0.04266	5455	0.674	0.693	0.626
30.746	0.825	0.04314	5588	0.693	0.714	0.643
29.483	0.467	0.04521	5700	0.758	0.776	0.701
29.920	0.821	0.04548	5789	0.763	0.783	0.702
30.396	0.818	0.04727	6077	0.820	0.840	0.755
30.559	0.816	0.04921	6348	0.885	0.904	0.818
30.494	0.813	0.05013	6458	0.924	0.947	0.842
30.654	0.814	0.05070	6554	0.938	0.960	0.872
30.722	0.810	0.05268	6820	1.009	1.032	0.938
30.779	0.807	0.05399	6998	1.060	1.082	0.980
30.912	0.803	0.05623	7309	1.146	1.171	1.063
30.754	0.797	0.05808	7524	1.224	1.249	1.129
31.165	0.793	0.06061	7919	1.327	1.353	1.230
31.307	0.789	0.06267	8213	1.414	1.440	1.297
31.380	0.783	0.06521	8559	1.521	1.552	1.380
31.447	0.777	0.06841	8992	1.666	1.698	1.501
31.500	0.770	0.07143	9399	1.806	1.842	1.631
31.418	0.763	0.07396	9715	1.928	1.964	1.742
31.408	0.752	0.07752	10180	2.104	2.145	1.900
26.404	0.744	0.08044	9483	2.302	2.342	2.093
24.902	0.739	0.08193	9337	2.397	2.435	2.166
24.208	0.730	0.08534	9572	2.595	2.638	2.348
24.855	0.724	0.08792	10009	2.737	2.781	2.501
30.037	0.725	0.08830	11267	2.686	2.728	2.451
26.638	0.715	0.09121	10808	2.905	2.956	2.637
28.418	0.705	0.09485	11688	3.096	3.151	2.819
29.592	0.696	0.09782	12363	3.257	3.313	2.968
30.337	0.685	0.10107	12977	3.443	3.505	3.142
16.632	0.140	0.10513	9801	4.029	4.077	3.569
15.554	0.147	0.11092	10055	4.451	4.505	3.942
15.068	0.157	0.11807	10567	4.988	5.057	4.433
14.979	0.166	0.12470	11134	5.505	5.581	4.908
14.807	0.166	0.12497	11107	5.530	5.609	4.919
15.004	0.177	0.13166	11764	6.065	6.149	5.416
15.840	0.188	0.13940	12732	6.693	6.782	6.003
17.283	0.199	0.14584	13826	7.195	7.299	6.459
18.604	0.213	0.15382	15078	7.918	8.032	7.123

T_{in} [°C]	p [bar]	Γ [kg/s]	Re	Δp_1 [kPa]	Δp_2 [kPa]	Δp_3 [kPa]
18.684	0.221	0.15961	15677	8.384	8.502	7.541
18.569	0.235	0.16661	16318	9.102	9.233	8.192
18.539	0.248	0.17391	17020	9.763	9.907	8.803
18.446	0.262	0.18062	17636	10.450	10.605	9.414
18.641	0.276	0.18789	18435	11.189	11.355	10.085
18.952	0.290	0.19457	19240	11.886	12.067	10.726
19.394	0.306	0.20177	20172	12.651	12.847	11.418
20.118	0.319	0.20856	21225	13.355	13.560	12.063
20.341	0.336	0.21529	22030	14.114	14.329	12.740
20.379	0.352	0.22240	22778	14.952	15.177	13.499
20.123	0.370	0.22942	23351	15.800	16.046	14.262
20.298	0.388	0.23646	24171	16.671	16.936	15.069
20.376	0.404	0.24285	24873	17.469	17.752	15.792
20.566	0.425	0.25060	25785	18.441	18.738	16.680
20.391	0.442	0.25662	26294	19.247	19.561	17.417
20.838	0.461	0.26370	27313	20.150	20.492	18.246
21.219	0.481	0.26989	28213	21.105	21.463	19.103
21.035	0.507	0.27791	28923	22.335	22.713	20.223

2. ADIABATIC TWO-PHASE PRESSURE DROPS

p [bar]	G [kg/m^{2}s]	x_{in}	Δp_{tot} [kPa]
28.99	192.8	0.083	28.971
30.02	188.6	0.190	31.207
29.41	189.5	0.191	31.592
28.73	194.5	0.323	38.710
28.21	192.2	0.347	39.064
28.71	195.2	0.437	50.647
29.26	195.7	0.537	62.871
29.14	194.4	0.535	63.099
28.83	191.7	0.673	78.184
28.72	194.0	0.762	89.959
28.51	187.6	0.805	86.712
28.73	191.3	0.874	90.103
28.64	191.0	0.876	89.885
28.48	195.0	0.947	86.392

p [bar]	G [kg/m^{2}s]	x_{in}	Δp_{tot} [kPa]
28.77	387.1	0.158	64.142
28.92	386.9	0.157	63.870
28.40	383.6	0.262	111.252
28.84	380.7	0.269	106.401
28.51	389.7	0.255	108.027
28.44	385.6	0.368	168.888
28.35	385.9	0.463	233.955
27.23	390.3	0.473	263.237
27.81	387.8	0.476	252.571
28.11	388.0	0.475	251.414
28.18	391.6	0.560	313.299
28.14	391.1	0.561	315.705
27.82	387.5	0.581	325.635
27.90	387.2	0.584	303.530
28.44	387.9	0.676	365.073
27.77	385.2	0.684	378.869
27.94	385.2	0.684	375.025
27.74	393.9	0.767	425.296
27.70	393.5	0.769	424.736
27.46	387.9	0.896	398.239
27.31	387.9	0.896	399.759
27.14	387.2	1.007	263.362
27.20	387.2	1.007	261.133
27.77	585.3	0.152	145.641
28.54	580.2	0.164	144.992
27.80	587.4	0.257	272.063
28.02	586.5	0.257	268.303
28.16	585.7	0.258	263.422
27.97	585.7	0.261	251.794
28.15	579.5	0.265	268.951
27.89	582.8	0.372	438.158
27.80	583.8	0.371	440.097
27.71	590.1	0.461	633.329
27.11	582.7	0.482	703.651
26.71	583.0	0.588	990.643
25.60	586.0	0.696	1029.036
25.87	586.6	0.699	1029.059

p [bar]	G [kg/m^{2}s]	x_{in}	Δp_{tot} [kPa]
40.30	195.1	0.136	29.824
39.49	191.9	0.149	28.772
38.96	193.6	0.148	28.511
38.80	190.2	0.261	30.526
38.78	193.4	0.250	30.680
38.57	191.0	0.367	32.268
38.85	190.3	0.369	32.106
38.88	195.0	0.460	39.271
39.06	194.7	0.462	38.789
38.83	193.7	0.570	48.903
38.80	193.9	0.669	58.635
38.74	190.7	0.793	65.716
38.66	193.2	0.876	69.730
38.62	193.9	0.973	64.786
38.62	392.3	0.146	53.564
39.17	391.3	0.146	51.869
38.65	390.8	0.167	50.138
38.48	394.2	0.243	82.274
38.49	394.6	0.242	81.205
38.69	393.8	0.243	80.453
39.35	389.2	0.273	75.643
38.82	382.2	0.290	80.485
38.80	390.9	0.272	79.029
38.66	388.6	0.381	118.224
38.55	389.5	0.379	119.081
38.54	388.8	0.491	167.767
38.48	388.7	0.491	167.147
38.26	390.1	0.597	218.316
38.13	390.4	0.672	263.917
37.88	389.4	0.783	290.699
37.71	385.1	0.906	269.834
38.90	581.8	0.158	109.520
37.99	582.0	0.268	197.795
38.30	580.7	0.269	193.764
38.50	580.2	0.268	192.918

p [bar]	G [kg/m^{2}s]	x_{in}	Δp_{tot} [kPa]
38.00	578.8	0.381	305.666
37.67	585.0	0.483	464.042
36.80	582.6	0.603	661.872
37.06	582.5	0.603	654.618
36.28	583.2	0.705	751.329
36.47	582.5	0.706	745.514
58.94	194.7	0.141	38.739
58.99	196.6	0.230	29.298
59.24	195.7	0.331	29.931
59.05	195.6	0.332	29.831
59.77	194.7	0.432	29.882
58.95	195.7	0.429	30.279
59.09	195.2	0.431	30.340
58.91	192.6	0.543	33.468
58.81	192.6	0.646	38.912
58.87	195.4	0.629	39.145
59.11	195.3	0.729	43.475
59.16	195.4	0.827	45.665
59.05	190.6	0.861	44.855
58.44	197.5	0.911	47.543
58.71	196.5	0.919	47.402
58.92	388.9	0.183	45.834
59.29	389.4	0.279	59.499
58.62	391.3	0.277	60.917
58.69	387.7	0.385	80.667
58.55	388.4	0.384	81.304
58.44	390.6	0.488	107.729
58.36	390.6	0.489	107.573
58.46	389.7	0.598	134.714
57.89	391.3	0.701	161.575
58.95	390.2	0.704	157.573
58.53	389.0	0.820	175.032
57.98	388.7	0.822	176.656
58.07	388.6	0.927	164.319
58.74	584.0	0.173	83.996

p [bar]	G [kg/m^{2}s]	x_{in}	Δp_{tot} [kPa]
58.69	582.2	0.175	84.717
58.74	581.1	0.176	86.316
59.11	578.1	0.287	128.132
58.66	581.2	0.283	130.463
58.55	582.0	0.282	131.364
58.09	586.2	0.383	196.141
57.87	587.4	0.383	196.773
57.83	582.7	0.498	286.696
57.91	582.5	0.499	286.486
57.86	580.1	0.621	385.022
57.40	578.9	0.686	412.314

3. DWO INSTABILITIES

P [bar]	G [kg/m^{2}s]	T_{in} [°C]	q [kW]	N_{sub}	N_{pch}
19.608	99.587	147.9	15.486	12.64	56.87
20.229	98.903	159.0	14.505	10.50	52.07
20.129	99.619	172.3	13.987	7.93	50.08
20.277	100.008	177.2	13.990	7.03	49.55
20.142	98.789	181.3	14.556	6.20	52.53
20.114	99.282	188.0	13.004	4.89	46.75
19.933	100.222	192.6	12.688	3.94	45.58
20.076	99.812	199.2	14.038	2.69	50.30
21.210	203.400	146.4	24.138	12.76	40.27
19.940	199.788	158.0	21.629	10.69	38.97
19.563	199.585	172.8	20.126	7.77	36.96
19.927	200.368	177.6	19.250	6.89	34.60
20.147	200.914	181.3	19.038	6.21	33.77
20.007	201.066	188.1	17.499	4.84	31.23
20.009	201.920	192.3	17.890	4.02	31.79
19.413	200.618	198.5	19.252	2.56	35.43
19.768	199.877	202.0	18.649	1.99	33.86
20.208	200.092	206.5	16.497	1.28	29.30
23.22	198.7	148.2	25.907	12.22	40.58
21.79	201.1	158.3	23.434	10.60	38.53

P [bar]	G [kg/m^{2}s]	T_{in} [°C]	q [kW]	N_{sub}	N_{pch}
19.29	201.1	170.3	21.289	8.22	39.32
19.54	203.4	181.5	18.936	6.03	34.17
22.34	201.5	188.5	18.404	5.33	29.50
22.80	200.3	197.5	16.802	3.84	26.57
20.27	197.2	204.9	20.174	1.63	36.26
19.42	199.2	208.0	18.655	0.61	34.56
21.13	195.7	198.4	18.485	3.20	32.17
21.32	200.2	205.7	18.507	1.89	31.22
20.92	398.3	148.0	55.880	12.49	48.24
20.09	398.6	155.8	51.298	11.10	45.99
21.15	398.4	168.5	48.605	8.75	41.51
21.25	399.1	180.1	48.630	6.64	41.28
21.65	398.5	191.3	53.311	4.67	44.51
21.76	397.9	200.0	45.874	3.10	38.18
22.61	397.3	207.8	35.874	1.97	28.83
20.39	397.6	205.1	38.776	1.65	34.36
22.63	601.1	132.8	90.967	14.88	48.26
21.20	601.0	147.3	91.073	12.59	51.44
21.54	599.3	158.0	86.227	10.66	48.10
22.44	600.3	170.3	83.567	8.51	44.77
20.88	599.7	180.8	88.609	6.44	50.90
20.76	599.8	191.3	78.012	4.43	45.05
21.22	599.6	197.8	71.197	3.34	40.28
20.50	599.0	203.9	61.086	1.92	35.75
21.57	599.4	207.7	54.574	1.61	30.40
21.44	604.1	133.2	89.052	15.08	49.51
21.30	603.6	120.7	91.581	17.32	51.27
9.998	199.125	139.749	14.876	14.85	51.57
9.483	199.453	144.551	13.876	12.86	50.46
9.882	201.504	149.646	13.324	11.16	46.15
10.312	200.844	156.241	13.755	9.05	45.93
9.579	200.815	160.068	12.317	6.98	44.07
9.775	200.510	165.860	11.497	4.99	40.43
10.075	201.228	169.983	13.277	3.82	45.22
9.773	200.495	175.248	10.400	1.42	36.58

P [bar]	G [kg/m^{2}s]	T_{in} [°C]	q [kW]	N_{sub}	N_{pch}
9.756	398.995	140.539	50.391	14.50	89.20
9.051	402.908	145.504	50.598	12.24	95.14
8.958	398.099	151.280	51.895	9.83	99.72
10.125	399.698	155.401	52.814	9.21	90.14
9.450	402.245	159.566	51.451	7.03	93.08
8.915	398.179	165.307	40.269	4.02	77.71
9.547	397.679	170.624	34.102	2.85	61.81
9.603	397.649	175.455	29.319	1.06	52.85

4. SYSTEM CHARACTERISTICS Γ-Δp

p [bar]	Γ [kg/h]	T_{in} [°C]	q [kW]	Δp_{tot} [kPa]
20.554	816.2	148.7	20.1	253.9
20.179	519.5	151.5	20.0	151.7
20.236	404.8	148.2	20.1	123.5
20.678	317.2	152.4	20.0	105.5
19.859	255.4	149.2	20.0	95.5
20.258	198.0	148.7	19.9	86.9
20.729	154.5	148.8	19.9	69.8
20.012	108.0	151.0	19.8	60.0
20.032	86.5	146.0	19.8	55.1
20.324	64.8	148.1	19.8	47.7
23.413	787.5	149.8	39.5	241.0
19.794	636.0	150.3	39.4	185.7
21.002	522.5	151.1	39.3	150.8
21.511	387.0	152.5	40.0	126.0
20.837	309.2	148.7	40.0	119.8
21.475	264.1	149.9	39.9	116.3
21.444	222.7	150.3	39.8	115.0
20.907	174.1	149.9	39.7	115.6
20.967	141.7	149.5	39.6	113.7
20.200	120.0	149.3	39.7	110.1
20.294	101.9	147.8	39.6	100.6
20.345	87.6	150.2	39.6	91.6

p [bar]	Γ [kg/h]	T_{in} [°C]	q [kW]	Δp_{tot} [kPa]
23.567	782.8	149.3	49.9	238.8
22.212	645.5	149.3	50.0	188.0
21.859	513.4	149.5	49.7	155.7
21.678	382.2	151.3	50.0	164.5
21.782	335.6	149.4	49.9	160.6
21.884	278.1	149.4	49.8	160.6
21.583	213.4	148.5	49.6	162.4
21.759	178.2	150.0	49.5	159.9
21.518	146.6	150.5	49.5	154.9
21.252	128.6	150.5	49.8	149.2
20.982	112.5	151.3	49.8	137.7
20.572	101.7	149.9	49.8	128.1
20.336	567.0	118.6	39.9	165.6
21.230	382.1	122.9	39.4	117.9
22.749	360.9	119.0	39.4	113.6
21.946	289.9	119.6	39.2	99.9
22.431	246.1	120.3	39.0	90.0
21.901	188.4	118.0	38.7	90.8
21.587	153.1	119.2	38.6	89.8
21.528	126.2	119.9	38.5	89.5
21.495	104.6	119.7	38.4	85.4
20.995	94.0	118.1	38.4	84.5
22.346	704.5	118.9	50.2	210.1
24.380	491.3	120.8	49.8	143.2
21.191	410.0	121.2	49.9	123.3
22.619	297.7	120.8	49.9	112.9
22.215	230.1	118.9	49.7	120.7
22.927	182.0	119.7	49.5	123.5
21.822	153.4	119.4	49.5	129.3
21.434	134.3	119.5	49.5	129.3
21.213	118.0	119.6	49.4	125.5
20.943	105.8	119.5	49.4	119.6
20.676	92.4	120.6	48.9	106.4
10.479	838.6	123.8	39.5	263.3
10.178	696.8	118.8	40.0	208.7

p [bar]	Γ [kg/h]	T_{in} [°C]	q [kW]	Δp_{tot} [kPa]
9.838	533.1	122.0	39.8	171.2
11.876	422.2	121.7	40.6	148.5
11.311	302.6	121.0	39.9	167.9
11.835	218.2	121.1	39.7	170.5
12.126	164.9	120.6	40.1	175.0
12.064	137.3	119.5	40.0	171.8
11.961	116.4	119.7	40.0	165.4
11.806	101.8	120.5	40.0	157.6
11.688	85.2	118.5	40.0	136.1
12.339	740.9	99.2	41.8	225.8
10.705	412.9	100.8	41.2	126.4
11.692	338.0	98.7	41.0	114.8
11.281	267.2	101.4	40.7	139.9
11.699	188.1	99.3	40.4	144.7
11.619	151.4	99.6	40.3	156.5
11.248	126.9	99.5	40.3	161.6
11.202	105.8	101.2	40.2	156.3
11.335	91.0	101.2	40.2	141.7
11.231	79.3	101.5	40.1	127.2
12.041	968.4	119.8	59.8	320.9
11.221	816.7	119.2	59.9	267.7
11.501	656.4	118.9	59.6	296.3
12.079	465.2	119.2	59.2	328.8
11.755	323.1	118.7	59.0	403.6
11.792	248.4	119.8	58.8	435.9
11.640	199.7	120.6	58.8	451.4
11.373	174.9	119.1	58.8	448.4
11.009	151.7	118.8	58.8	433.7
41.761	508.6	121.4	60.0	145.0
40.397	381.0	119.2	59.5	115.9
40.276	282.5	117.8	59.2	99.6
42.015	235.1	119.9	59.4	97.6
38.979	208.7	120.5	59.2	106.5
41.033	158.9	122.9	58.9	96.9
41.180	158.8	120.6	59.8	102.2

p [bar]	Γ [kg/h]	T_{in} [°C]	q [kW]	Δp_{tot} [kPa]
38.883	137.7	119.3	59.8	102.7
39.883	119.5	120.4	60.0	95.9
39.506	114.2	121.8	60.0	93.6
39.862	404.6	122.4	50.0	121.4
41.479	308.5	120.7	49.8	101.4
40.578	240.6	121.4	49.9	86.7
40.620	197.7	118.9	49.7	83.1
41.634	165.4	121.1	49.4	80.4
40.187	138.4	122.0	49.2	79.7
41.147	125.5	121.3	49.1	76.3
40.936	107.1	123.4	49.0	73.1
41.001	100.5	119.3	48.9	70.8
40.545	85.6	119.8	48.9	64.7

5. LEDINEGG INSTABILITIES

p [bar]	G [kg/m^{2}s]	T_{in} [°C]	q [kW]	N_{sub}	N_{pch}
21.27	596.3	111.7	41.92	18.92	23.79
20.90	605.6	121.1	39.41	17.38	22.39
21.30	601.8	126.9	39.31	16.22	22.07
21.07	590.7	137.3	36.34	14.42	21.01
21.81	593.0	145.4	36.29	12.88	20.23
21.66	594.2	145.5	71.37	12.86	39.95
22.28	593.3	137.6	80.92	14.14	44.16
21.65	599.0	128.0	81.23	15.95	45.11
21.69	597.7	122.6	83.60	16.87	46.47
21.83	592.8	113.3	86.38	18.44	48.11
21.18	602.4	127.9	89.85	16.07	50.68
20.51	607.7	121.7	91.08	17.40	52.50
20.72	601.0	112.3	91.23	19.03	52.68
10.66	401.5	99.8	24.95	28.58	40.39
10.60	403.5	108.0	24.92	25.83	40.35
10.59	402.7	119.5	22.21	21.94	36.08
10.46	399.2	130.9	27.08	18.02	44.88
10.45	400.3	130.6	37.11	18.14	61.41

p [bar]	G [kg/m^{2}s]	T_{in} [°C]	q [kW]	N_{sub}	N_{pch}
10.72	400.0	119.4	42.01	21.91	67.93
10.81	398.3	109.8	47.17	25.07	76.01
11.00	393.7	101.5	49.47	27.66	79.34
10.13	413.6	117.2	54.66	22.98	90.13
10.39	408.7	107.7	54.44	26.13	88.69
10.12	414.7	97.9	59.71	29.83	98.33
19.77	402.6	100.3	37.22	21.67	33.54
20.60	404.8	119.8	34.01	17.71	29.32
20.50	400.7	121.6	56.22	17.41	49.19
20.16	395.5	101.4	58.90	21.29	53.06
20.51	400.9	121.7	58.83	17.40	51.41
20.21	399.3	140.6	56.19	13.96	50.01

CURRICULUM SCIENTIFICO DEL GRUPPO DI RICERCA

Il gruppo di lavoro impegnato nell'attività è costituito da un professore ordinario di Impianti Nucleari del Politecnico di Milano (Dipartimento Energia), Marco Enrico Ricotti, da un ricercatore dello stesso Dipartimento, Antonio Cammi, e da due dottorandi, Marco Colombo e Jacopo De Amicis.

Il prof. Ricotti e il prof. Cammi svolgono attività di ricerca da oltre 15 anni al Politecnico nel campo della Ingegneria Nucleare, con particolare riferimento alla termoidraulica, alla sicurezza, agli aspetti economici dell'energia nucleare ed hanno svolto o coordinato ricerche teorico-modellistiche e sperimentali nel gruppo Reattori Nucleari del Dipartimento di Energia del Politecnico di Milano, pubblicando i risultati su rivista e in atti di Congresso, quasi esclusivamente internazionali. Sono autori di diversi rapporti nell'ambito dei PAR trascorsi.

L'ing. Colombo e l'ing. De Amicis sono dottorandi del Politecnico di Milano e stanno svolgendo le rispettive ricerche nell'ambito del Dottorato in Scienza e Tecnologie Energetiche e Nucleari, sulle tematiche teorico-modellistiche e sperimentali che sono oggetto del presente rapporto. Anch'essi sono autori di paper scientifici pubblicati su rivista o presentati a congressi internazionali.

Maggiori dettagli sulle attività di ricerca nonché l'elenco delle pubblicazioni più recenti si possono trovare sul sito Web del gruppo di ricerca del Politecnico di Milano (http://www.nuclearenergy.polimi.it).